



北京大学

# 本科生毕业论文

题目：转角双层二硒化钨中的超导性

---

姓 名： 陈沫阳

学 号： 2100011462

院 系： 物理学院

专 业： 物理学

指导教师： B.Andrei.Bernevig

二〇二五年五月



## 版权声明

任何收存和保管本论文各种版本的单位和个人，未经本论文作者同意，不得将本论文转借他人，亦不得随意复制、抄录、拍照或以任何方式传播。否则一旦引起有碍作者著作权之问题，将可能承担法律责任。



## 摘要

超导态作为量子物质凝聚的宏观体现，其零电阻与完全抗磁性特征自 1911 年发现以来持续推动着凝聚态物理的发展。传统 BCS 理论虽成功阐释声子媒介的库珀配对机制，却无法解释铜基与铁基高温超导体等超越麦克米兰 (McMillan) 极限或说不仅仅受电声耦合调制的非常规行为。这些材料中强电子关联、自旋涨落与竞争序的复杂相互作用，亟需新的研究平台突破理论困境。近年来，以转角二维石墨烯为代表的二维转角材料通过转角调控或者其它手段实现关联量子相，为研究强关联物理提供了全新视角与平台。魔角石墨烯体系虽展现出拓扑平带与非常规超导等特性，但其弱自旋-轨道耦合与缺乏谷自由度限制了其模拟高温超导微观机制的能力。本论文聚焦新兴的过渡金属二硫化物 (TMD) 的转角双层体系，以  $3.65^\circ$  转角双层二硒化钨 ( $t\text{WSe}_2$ ) 为研究对象，通过发展构建基于第一性原理的连续模型的系统方法，结合对于有限温下正常态的哈特里-福克 (Hartree-Fock) 平均场自洽计算，复现了实验中出现的现象，验证了模型的可靠性，为下一步系统揭示其非常规超导的微观起源与调控机制提供了基础，让进一步的深入研究成为了可能。

论文首先讨论二维超导研究的理论框架，讨论描述超导相变的理论。我们从传统 BCS 理论出发，推导声子所诱导的有效吸引势与 Bogoliubov-de Gennes 哈密顿量，简要阐明传统超导体的能隙形成机制及其对费米面附近态密度的依赖性。结合 Ginzburg-Landau 唯象理论，分析超导体中的涡旋形成条件与磁通穿透行为，揭示  $\kappa$  参数对超导类型划分的物理内涵，跳出迈斯纳效应中完美抗磁性的束缚。针对二维体系的特殊性，我们深入讨论了 Berezinskii-Kosterlitz-Thouless (BKT) 拓扑相变理论：通过二维 XY 模型刻画涡旋-反涡旋对的结合与解离过程，阐明准长程序与拓扑缺陷的竞争关系，同时我们立足实验，导出了相变临界点附近可能的电压-电流关系。在这一章的理论分析不仅介绍了传统超导研究的理论框架，更为后续转角体系的低维超导行为分析奠定基础。

针对转角材料解析连续模型的建模难题，论文第三章系统介绍了基于第一性原理的普适性连续模型构建方法。通过缜密分析 AA/AB 堆垛构型，我们从两个方法导出了转角材料的层间跃迁矩阵。其一是使用二中心近似 (two-center approximation)，直接导出层间跃迁矩阵。第二种方法，也是我们认为与第一种方法异曲同工但更加普适的方法，是结合 moiré 超晶格平移对称性与空间旋转对称性 (如  $C_{3z}, C_{2y}\mathcal{T}$  等)，建立 K 谷低能有效哈密顿量的通用表达式。这种基于近似成立的对称性约束直接推导出连续波形表达式的方法，有利于我们研究多参数高精度的连续模型。我们进一步引入高阶谐波项与梯度项，构建高精度“DFT 模型”，其能带结构较传统二阶谐波模型 (second harmonic model) 更贴合原子尺度计算结果。区别于传统经验拟合策略，直接从密度泛函理论 (DFT) 数据提取有效质量、跃迁系数等参数，可以确保模型在转角与堆垛构型间的可迁移性，是一个系统化的构造方法。该方法突破传统 Bistritzer-MacDonald 模型，实现了对 TMD 转角双层体系以及其它转角体系的微观描述，为强关联相变研究提供可靠的理论工具。

基于上述方法，论文第四章开始系统研究  $3.65^\circ t\text{WSe}_2$  中的量子相变。在第一节里我们简单介绍了近期报告发现  $3.65^\circ t\text{WSe}_2$  中超导性的实验。我们将实验现象与第二章中介绍的 BKT 相变理论联系起来，说明  $t\text{WSe}_2$  中的超导性符合一般二维超导体的共性。下面我们开始介绍我们对  $3.65^\circ t\text{WSe}_2$  的数值模拟工作的基础。我们基于第三章介绍的方法，构建了一个  $t\text{WSe}_2$  的连续模型，并加入了双栅极屏蔽库伦势 (double-gated screened Coulomb potential) 以描述电子相互作用。接着，我们把哈

密顿量投入到有限个能带组成的基底之下，并对其做平均场近似。在这之后，我们结合自洽哈特里-福克方法，发现位移场调控下关联绝缘体-金属的量子相变路径。在强相互作用区域，体系以铁磁相主导的谷极化态为特征，自旋能隙的打开昭示了铁磁相的鲁棒性；在弱关联区域，也是相变符合实验现象的区域，谷间相干序（intervalley coherence order）驱动的平移对称性破缺态逐渐占据主导，伴随动量空间嵌套矢量相关的电荷密度波形成。模拟计算预测的谷间相干序与实验发现一致，考虑到转角二硫化物材料的强自旋-谷耦合，这可能揭示了自旋涨落在超导非常规配对机制的潜在作用。在本章最后一节，通过对比现在广泛使用的二阶谐波模型，我们展示了本研究使用的 DFT 模型在能隙与相图预测能力上展现显著优势。在论文的第五章，我们回顾了文章的讨论，说明了已有的结论，并对进一步的研究提出了规划与展望。

本研究的核心创新在于建立基于 ab-initio 数据构造的转角双层连续模型，阐明 moiré 周期势、强自旋-轨道耦合与库仑相互作用的协同调控机制，为进一步研究研究非常规超导性打下了坚实的基础。理论预测的相图演化规律为“转角工程”的设计提供新思路：通过位移场调节层间杂化强度，可实现从关联金属态、关联绝缘态到超导态的连续调控；结合压力与电场多维手段，有望在二维极限下探索高温超导的普适相图，寻找超越电声耦合的超导配对机制。此外，在进行自洽计算的过程中，我们考虑了多种破坏 moiré 平移对称性的态，包括有 IVC 序的态，有电荷密度波序的态，有凯库勒螺旋序态（Kekulé spiral ordered states）。这些都可推广至其他转角 TMD 体系连续模型的构建与计算中（如 MoTe<sub>2</sub>、WS<sub>2</sub>等），为理解非常规超导机制及设计新型量子材料提供理论范式。

关键词：超导性；转角材料；过渡金属二硫化物；第一性原理计算

## Superconductivity in Twisted Bilayer WSe<sub>2</sub>

Mu-Yang Chen (Physics)

Directed by B.Andrei.Bernevig

### ABSTRACT

Superconductivity, as a macroscopic manifestation of quantum matter, has driven the development of condensed matter physics since its discovery in 1911. While the conventional BCS theory successfully explains the phonon-mediated Cooper pairing mechanism, it fails to account for unconventional superconductors like cuprates and iron-based materials that surpass the McMillan limit and involve mechanisms beyond electron-phonon coupling. The complex interplay of strong electronic correlation, spin fluctuation, and competing orders in these materials demands new research platforms to overcome theoretical challenges. Recently, twisted two-dimensional materials represented by magic angle graphene have emerged as novel platforms for studying strongly correlated physics through twist angle engineering. This thesis focuses on emerging twisted transition metal dichalcogenide (TMD) bilayers, particularly 3.65° twisted tungsten diselenide (tWSe<sub>2</sub>). By developing a systematic ab-initio based continuum modeling approach combined with finite temperature Hartree-Fock self consistent calculations for the normal states, we successfully reproduced some experimental observations and validated the model's reliability, laying the foundation for systematically revealing the microscopic origin and regulation mechanisms of unconventional superconductivity.

The thesis first establishes the theoretical framework for 2D superconductivity, while also discussing the BCS theory. This theoretical foundation supports subsequent analysis of low-dimensional superconducting behaviors in twisted systems. Addressing modeling challenges in twisted materials, Chapter 3 introduces a universal continuum model construction method, enabling systematic studies with high precision "DFT models" that incorporate higher order harmonic and gradient terms. Chapter 4 investigates quantum phase transitions in 3.65° tWSe<sub>2</sub>. Besides connecting experimental observations of superconductivity with BKT transition theory, we construct a continuum model incorporating double-gated screened Coulomb interaction. Through mean-field approximation and self-consistent Hartree-Fock calculations, we reveal an insulator-metal transition pathway, aligning well with the experimental facts. The last chapter concludes all the content and gives a brief outlook.

KEY WORDS: Superconductivity ; Twisted Materials ; Transition Metal Dichalcogenides ; First Principle Calculation

## 目录

<b>第一章 Introduction</b>	<b>1</b>
<b>第二章 Superconductivity</b>	<b>3</b>
2.1 BCS Theory . . . . .	3
2.1.1 Attractive Interaction Induced by Phonon . . . . .	3
2.1.2 BdG Hamiltonian . . . . .	5
2.1.3 Vortices in Superconductors . . . . .	6
2.2 BKT Phase Transition . . . . .	8
2.2.1 2D Classical XY Model . . . . .	10
2.2.2 Vortices in XY Model . . . . .	11
2.2.3 Voltage-Current Relation Near the Critical Point . . . . .	13
<b>第三章 Constructing Continuum Models</b>	<b>15</b>
3.1 Stacking Configurations and Interlayer Hopping . . . . .	16
3.1.1 AA Stacking . . . . .	16
3.1.2 AB Stacking . . . . .	18
3.2 General Method to Obtain Continuum Model . . . . .	19
3.2.1 Symmetry and Basic Notation . . . . .	20
3.2.2 Second Harmonic Model and General Expression . . . . .	21
3.2.3 Obtaining Parameters from ab-initio Calculation . . . . .	23
<b>第四章 Superconductivity in <math>3.65^\circ</math> tWSe<sub>2</sub></b>	<b>25</b>
4.1 Experimental Motivation and Unconventional Signals . . . . .	25
4.2 Self consistent HF results for $\theta = 3.65^\circ$ tWSe <sub>2</sub> . . . . .	27
4.2.1 Interaction in continuum model . . . . .	28
4.2.2 Mean Field Approximation . . . . .	30
4.2.3 Hartree Fock Potential . . . . .	31
4.2.4 Numerical results of $\nu = -1$ tWSe <sub>2</sub> Based on DFT Model . . . . .	33
4.2.5 Benchmark . . . . .	37
<b>第五章 Conclusion and Outlook</b>	<b>39</b>
<b>参考文献</b>	<b>41</b>

致谢	45
北京大学学位论文原创性声明和使用授权说明	47

## 第一章 Introduction

The pursuit of superconductivity—a quantum state of matter characterized by zero electrical resistance and diamagnetism—has driven condensed matter physics for over a century. Since its serendipitous discovery in mercury by Heike Kamerlingh Onnes in 1911, superconductivity has evolved from a laboratory curiosity to a cornerstone of modern physics and technology. The Bardeen-Cooper-Schrieffer (BCS) theory<sup>[1]</sup>, formulated in 1957, elegantly explained conventional superconductivity through phonon-mediated Cooper pairing, yet it could not account for the emergence of high-temperature superconductivity in cuprates and iron-based compounds<sup>[2]</sup> which are far beyond the higher bound of the critical temperatures in BCS theory, i.e. the Macmillan limit<sup>[3]</sup>. These unconventional superconductors, with their complex interplay of strong electron correlation, spin fluctuation, and competing orders, have defied a universal theoretical framework, motivating the search for new platforms to decode the enigmatic mechanisms behind high temperature superconductors.

In recent years, physicists have witnessed an explosive progress in the research of twisted materials. The emergence of "twistronics"—the manipulation of interlayer twist angles in stacked 2D materials—has unlocked unprecedented control over electronic correlations. In the family of twisted materials, twisted bilayer graphene(TBG) is the most famous one. People's interest in this fancy material has been developing since more than twenty years ago, and now the study of twisted bilayer graphene<sup>[4][5]</sup> is still one of the most popular research topics. Moreover, the discovery of magic angle twisted bilayer graphene (MATBG) have caught numerous eyes of people. To be more specific, people find that the twisted bilayer graphene near a magic angle become a strongly correlated material instead of a system with only weak electronic interaction which can be described by Landau Fermi liquid. A lot of nontrivial phases appear near the magic angle, including superconducting states<sup>[6]</sup>, Mott insulating states, quantum anomalous Hall states<sup>[7]</sup> (states with nonzero Chern numbers), fragile topological states<sup>[8][9][10]</sup> and incommensurate Kekulé spiral(IKS) states<sup>[11]</sup>. With all those strongly correlated phases, the magic angle twisted bilayer graphene provides researchers with an appropriate platform to tune the electron correlation in experiments. Particularly, the superconductivity observed in TBG is beyond the frame of conventional superconductors mediated by electron-phonon coupling and is more similar to the high temperature superconductors like cuprate superconductors and iron-based superconductors<sup>[12]</sup>.

Transition metal dichalcogenides (TMDs), with the chemical formula  $\text{MX}_2$  ( $\text{M}$  = transition metal,  $\text{X}$  = chalcogen), are layered materials exhibiting diverse electronic phases<sup>[13]</sup>. While twisted bilayer graphene has revolutionized the study of correlated quantum phases in moiré systems, twisted transition metal dichalcogenides (TMDs) offer a distinct and equally rich platform for exploring new physics. Unlike graphene's semi-metallic Dirac bands, TMDs such as  $\text{WSe}_2$  and  $\text{MoTe}_2$  exhibit layer-dependent electronic structures, strong spin-orbit coupling (SOC) leading to the so-called "spin valley coupling", and valley-selective optical responses, making them uniquely suited for investigating spin-valley correlated states, topological superconductivity<sup>[14][15]</sup>, charge density wave<sup>[16]</sup>, magnetism<sup>[17]</sup> and moiré enhanced excitonic phenomena<sup>[18]</sup>. Among the topological states, the exciting observation of fractionally quantized anomalous quantized Hall states<sup>[19]</sup> in twisted bilayer  $\text{MoTe}_2$  ( $t\text{MoTe}_2$ ) arouses people's interest in twisted TMDs. Besides, recent paper<sup>[20]</sup> reported the unconventional superconductivity in twisted bilayer  $\text{WSe}_2$  at the  $3.65^\circ$  twist angle, which makes it possible for physicists to dive into the mechanism behind unconventional superconductivity in the family of twisted bilayer TMDs.

To investigate the physics in TMDs materials, people favor the large scale first principle study based on the density functional theory, demonstrating the band structures of corresponding materials. However, the ab-initio calculation itself is not sufficient for the cases when the strong correlation in moiré can not be neglected, such as the Mott insulating states and superconducting states. Thus we need the analytical single particle model to perform further investigation of those emergent strongly correlated phases. In this article, we introduce a systematic method to derive a continuum model for the moiré materials without fitting of band structures, illuminating a promising way to construct a model which aligns well with the details of ab-initio calculations.

The rest of our article is organized as follows: the second chapter gives a brief introduction of superconductivity, discussing both the BCS theory and Ginzburg-Landau theory of the conventional superconductors, while the Berezinskii-Kosterlitz-Thouless (BKT) description of quantum phase transitions is also included to better show the physics of two dimensional superconductors. The third chapter is about the methodology to construct a continuum model based on ab-initio calculation. We will first show the derivation of Bistritzer-MacDonald(BM) model, after we discuss the construction of models in a more general form. The fourth chapter talks about the recent experimental evidence of superconductivity in  $3.65^\circ$   $t\text{WSe}_2$ , and we exhibit our numerical study of  $3.65^\circ$   $t\text{WSe}_2$  at a specific hole filling factor based on our continuum model (DFT model). The last chapter is about the conclusion and outlook of our discussion.

## 第二章 Superconductivity

In this chapter, we will firstly discuss the well-known BCS theory of superconductivity, deriving some key features of the electron-phonon mediated superconductivity. After that, we will show the relation between Ginzburg-Landau phenomenological theory and the microscopic BCS theory, and use the Ginzburg-Landau theory to uncover the mechanism behind some interesting phenomena, such as the vortices in conventional superconductors. Our next step is to dive into the superconductivity in two-dimensional materials and give a heuristic introduction to the Berezinskii–Kosterlitz–Thouless (BKT) transition, which plays a crucial role in the theory of superconductor-insulator phase transition observed in two-dimensional systems.

### 2.1 BCS Theory

#### 2.1.1 Attractive Interaction Induced by Phonon

In this subsection, we will give a terse and concise derivation of the effective attractive interaction mediated by electron-phonon coupling. The Hamiltonian of the electron-phonon coupling system can be written as:

$$H = \sum_{\mathbf{k}, \sigma} (\epsilon_{\mathbf{k}} - \epsilon_F) \psi_{\mathbf{k}, \sigma}^\dagger \psi_{\mathbf{k}, \sigma} + \sum_{\mathbf{q}, \mu} \omega_{\mathbf{q}} b_{\mathbf{q}, \mu}^\dagger b_{\mathbf{q}, \mu} + \lambda \int_{\mathbf{r}} \rho(\mathbf{r}) \nabla \cdot \mathbf{u}(\mathbf{r}) + H_{int} \quad (2.1)$$

where  $\mathbf{q}$ ,  $\mathbf{k}$  denote the momentum, the  $\epsilon_k$  is the kinetic energy,  $\epsilon_F$  is the Fermi energy,  $\psi_{\mathbf{k}, \sigma}^\dagger$  is the creation operator of electrons while the index  $\sigma$  represents the spin index,  $b_{\mathbf{q}, \mu}^\dagger$  is the creation operator of a phonon and  $\mu$  is the direction index(x,y,z). Note that for theoretical simplicity, we assume that the phonon dispersion is irrelevant to the direction of lattice vibration. For the rest terms in the Hamiltonian Eq. (2.1),  $H_{int}$  describes the interaction between electrons,  $\lambda$  is the electron-phonon coupling constant,  $\rho$  is the electron density and  $\mathbf{u}(\mathbf{r})$  is the lattice displacement field at position  $\mathbf{r}$ . Using the relation between phonon and Fourier components of the lattice displacement field:

$$u_{\mathbf{q}, \mu} = \frac{i}{\sqrt{2m\omega_{\mathbf{q}}}} (b_{-\mathbf{q}, \mu}^\dagger + b_{\mathbf{q}, \mu}) \quad (2.2)$$

thus we are able to write down the action in the path integral expression of the partition function  $\mathcal{Z} = \int \mathcal{D}[\bar{\psi}, \psi] \mathcal{D}[b^*, b] e^{-S}$ . Introducing the Grassmann number  $\psi$  and complex number  $b$  to

characterize the fermionic coherent states and bosonic coherent states respectively, we have

$$S = S_{int} + \sum_{\mathbf{k}, n\sigma} \bar{\psi}_{\mathbf{k}, n, \sigma} (-i\omega_n + \epsilon_{\mathbf{k}} - \epsilon_F) \psi_{\mathbf{k}, n, \sigma} + S_{phonon} \quad (2.3)$$

and  $S_{phonon}$  is

$$\sum_{l, \mathbf{q}, \mu} b_{\mathbf{q}, l, \mu}^* (-i\omega_l + \omega_{\mathbf{q}}) b_{\mathbf{q}, l, \mu} + \lambda \sum_{\mathbf{q}, l, \mu} \frac{i q_{\mu}}{\sqrt{2m\omega_{\mathbf{q}}}} (b_{\mathbf{q}, l, \mu} + b_{-\mathbf{q}, l, \mu}^*) \rho_{-\mathbf{q}, l} \quad (2.4)$$

, in which  $\omega_n$  is the fermionic Matsubara frequency,  $\omega_l$  is the bosonic Matsubara frequency and  $\rho_{\mathbf{q}}$  can be expressed as the summation of  $\bar{\psi}_{\mathbf{k}+\mathbf{q}, n, \sigma} \psi_{\mathbf{k}, n, \sigma}$ . We can fully simplify the expression of  $S_{phonon}$  by defining:

$$\Omega_{\mathbf{q}, l, \mu} = \begin{pmatrix} -i\omega_l + \omega_{\mathbf{q}} & 0 \\ 0 & i\omega_l + \omega_{\mathbf{q}} \end{pmatrix}, \rho_{\mathbf{q}, l, \mu} = \begin{pmatrix} \frac{-i\lambda q_{\mu}}{\sqrt{2m\omega_{\mathbf{q}}}} \rho_{\mathbf{q}, l} \\ \frac{i\lambda q_{\mu}}{\sqrt{2m\omega_{\mathbf{q}}}} \rho_{\mathbf{q}, l} \end{pmatrix}, \mathbf{b}_{\mathbf{q}, l, \mu} = \begin{pmatrix} b_{\mathbf{q}, l, \mu} \\ b_{-\mathbf{q}, -l, \mu}^* \end{pmatrix} \quad (2.5)$$

we are now able to transform the  $S_{phonon}$  into a form which is easier for us to complete the square:

$$S_{phonon} = \frac{1}{2} \sum_{\mathbf{q}, l, \mu} \left( \mathbf{b}_{\mathbf{q}, l, \mu}^\dagger \Omega_{\mathbf{q}, l, \mu} \mathbf{b}_{\mathbf{q}, l, \mu} + \mathbf{b}_{\mathbf{q}, l, \mu}^\dagger \cdot \rho_{\mathbf{q}, l, \mu} + \rho_{\mathbf{q}, l, \mu}^\dagger \cdot \mathbf{b}_{\mathbf{q}, l, \mu} \right) \quad (2.6)$$

To analyze the dynamics of electrons, we integrate over the phonon's degrees of freedom so that we are able to obtain the effective field theory of electrons. Our scheme is to do variable substitution and then drop the terms irrelevant to electrons in the full action. In this way, the action of our theory is simplified to

$$S = S_{int} + \sum_{\mathbf{k}, n\sigma} \bar{\psi}_{\mathbf{k}, n, \sigma} (-i\omega_n + \epsilon_{\mathbf{k}} - \epsilon_F) \psi_{\mathbf{k}, n, \sigma} - \frac{1}{2} \sum_{\mathbf{q}, l, \mu} \rho_{\mathbf{q}, l, \mu}^\dagger \Omega_{\mathbf{q}, l, \mu} \rho_{\mathbf{q}, l, \mu} + S'_{phonon} \quad (2.7)$$

in which  $S'_{phonon}$  is the part we will throw away. Here we show the explicit form of effective action:

$$S_e = \sum_{\mathbf{k}, n\sigma} \bar{\psi}_{\mathbf{k}, n, \sigma} (-i\omega_n + \epsilon_{\mathbf{k}} - \epsilon_F) \psi_{\mathbf{k}, n, \sigma} + \sum_{\mathbf{q}, l} \left[ V(\mathbf{q}) - \frac{1}{2} \frac{\lambda^2 q^2}{2m(\omega_l^2 + \omega_{\mathbf{q}}^2)} \right] \rho_{\mathbf{q}, l} \rho_{-\mathbf{q}, -l} \quad (2.8)$$

and  $V(\mathbf{q})$  is the Fourier component of Coulomb interaction. Therefore, the effective potential including electron-phonon coupling is

$$V_{eff}(\mathbf{q}) = V(\mathbf{q}) - \frac{1}{2} \frac{\lambda^2 q^2}{2m(\omega_l^2 + \omega_{\mathbf{q}}^2)} \rho_{\mathbf{q}, l} \rho_{-\mathbf{q}, -l} \quad (2.9)$$

The phonon frequency actually has a natural ultraviolet cutoff-the Debye frequency  $\omega_D$ , and after applying Wick rotation  $\omega_l = -i\omega$  the denominator of electron-phonon coupling potential

becomes proportional to  $\omega_q^2 - \omega^2$ . Thus we can see it clear that the coupling leads to an attractive potential when  $\omega < \omega_D$ , making it possible to get an attractive effective potential for electrons, which is the core in BCS theory.

### 2.1.2 BdG Hamiltonian

In this subsection, we will give a short review of BCS theory. With the conclusion discussed in the previous subsection, now we start from the Hamiltonian with effective attraction (approximate to be momentum-independent):

$$H = \sum_{\mathbf{k}\sigma} \xi_{\mathbf{k}} n_{\mathbf{k},\sigma} - \frac{g}{\Omega} \sum_{\mathbf{k},\mathbf{k}',\mathbf{q}} \psi_{\mathbf{k}+\mathbf{q},\uparrow}^\dagger \psi_{-\mathbf{k},\downarrow}^\dagger \psi_{-\mathbf{k}'+\mathbf{q},\downarrow} \psi_{\mathbf{k}',\uparrow} \quad (2.10)$$

$\xi_{\mathbf{k}} = \epsilon_{\mathbf{k}} - \mu$  ( $\mu$  represents chemical potential),  $\psi^\dagger$  is the creation operator of electrons in this effective Hamiltonian and  $\Omega$  is the total area. The most well-known way to deal with this Hamiltonian is to apply mean field approximation and derive a self-consistent single particle level Hamiltonian. The mean field approach will be thoroughly discussed in chapter 四, so here we just skip the process and simply show the mean field Hamiltonian. We keep only the "superconductivity channel" in our mean-field Hamiltonian, postulating there exists a macroscopic number of Cooper pairs in the BCS ground state  $|GS\rangle$  so the order parameter

$$\Delta(\mathbf{q}) = \frac{g}{\Omega} \sum_{\mathbf{k}} \langle GS | \psi_{-\mathbf{k},\downarrow} \psi_{\mathbf{k}+\mathbf{q},\uparrow} | GS \rangle \quad (2.11)$$

and its conjugate  $\bar{\Delta}$  are non-zero in superconducting states. To further simplify our discussion, we neglect the momentum-dependence of the order parameter, i.e.  $\Delta(\mathbf{q}) \approx \Delta$ . Thus the mean field Hamiltonian is

$$H_{MF} = \sum_{\mathbf{k},\sigma} n_{\mathbf{k},\sigma} \xi_{\mathbf{k}} - (\Delta \sum_{\mathbf{k}} \psi_{\mathbf{k}\uparrow}^\dagger \psi_{-\mathbf{k}\downarrow}^\dagger + h.c.) + Const \quad (2.12)$$

Additionally, our mean field Hamiltonian can be written in a more compact form preserving particle-hole symmetry if we utilize the Nambu spinor  $\Psi_{\mathbf{k}} = \begin{pmatrix} \psi_{\mathbf{k}\uparrow} \\ \psi_{-\mathbf{k}\downarrow}^\dagger \end{pmatrix}^T$ :

$$H_{BdG} = \sum_{\mathbf{k}} \Psi_{\mathbf{k}}^\dagger \begin{pmatrix} \xi_{\mathbf{k}} & -\Delta \\ -\bar{\Delta} & -\xi_{\mathbf{k}} \end{pmatrix} \Psi_{\mathbf{k}} + Const = \sum_{\mathbf{k}} \Psi_{\mathbf{k}}^\dagger h_{BdG} \Psi_{\mathbf{k}} + Const \quad (2.13)$$

which is called the Bogoliubov de-Gennes Hamiltonian. Hamiltonian in this matrix form can be easily diagonalized with the following parameterized unitary transformation:

$$\begin{pmatrix} \gamma_{\mathbf{k}\uparrow} \\ \gamma_{-\mathbf{k}\downarrow}^\dagger \end{pmatrix} = \begin{pmatrix} \cos \theta_{\mathbf{k}} & \sin \theta_{\mathbf{k}} \\ \sin \theta_{\mathbf{k}} & -\cos \theta_{\mathbf{k}} \end{pmatrix} \Psi_{\mathbf{k}} = U_{\mathbf{k}} \Psi_{\mathbf{k}} \quad (2.14)$$

and the parameter  $\theta_{\mathbf{k}} = \frac{-1}{2} \arctan\left(\frac{\Delta}{\xi_{\mathbf{k}}}\right)$  while the eigenvalues are given by  $\pm\lambda_{\mathbf{k}} = \pm\sqrt{\Delta^2 + \xi_{\mathbf{k}}^2}$ . Hence our order parameter actually has another important meaning: the lower bound of the excitation gap  $\lambda_{\mathbf{k}}$ . In other words, when the order parameter  $\Delta$  is zero, superconductivity also disappears since there will be no energy cost of excitation and perturbation can easily break the Cooper pairs. To evaluate the order parameter, we go back to its definition in order to find the self-consistent relation. We begin with the explicit expression of the BCS ground state and  $|0\rangle$  is the vacuum state

$$|BCS\rangle = \prod_{\mathbf{k}} \gamma_{\mathbf{k}\uparrow} \gamma_{-\mathbf{k}\downarrow} |0\rangle \quad (2.15)$$

$$\Delta = \frac{g}{\Omega} \sum_{\mathbf{k}} \langle BCS | \psi_{-\mathbf{k}\downarrow} \psi_{\mathbf{k}+\mathbf{q}\uparrow} | BCS \rangle = \frac{g}{\Omega} \sum_{\mathbf{k}} \frac{\Delta}{2\lambda_{\mathbf{k}}} \quad (2.16)$$

Then we can find a significant conclusion (already using the energy cutoff  $\omega_D$ ):

$$\Delta = 2\omega_D e^{-\frac{1}{gN(\epsilon_F)}} \quad (2.17)$$

where  $N(\epsilon_F)$  is the density of states near the Fermi surface. Through Eq. (2.17), we can see it clear that superconductivity favors the systems possessing a large density of states near the Fermi surfaces to get a large gap so that we can stabilize the superconducting states. BCS theory is very successful in the prediction of conventional s-wave superconductors, however, as we will see soon, this powerful theory fails in dimensions lower than two. Moreover, electron-phonon coupling is only one of the mechanisms dominating superconducting states. Other kinds of mechanisms, such as spin fluctuation induced superconductivity<sup>[21]</sup>, charge density wave<sup>[22]</sup>, heavy fermion superconductor<sup>[23]</sup> and topological superconductor<sup>[24][25]</sup> should not be neglected in the pursuit of unconventional superconductors.

### 2.1.3 Vortices in Superconductors

To make the introduction of the general theory of two dimensional superconductors convenient, in this subsection we will digress to Ginzburg-Landau theory, using this phenomenological theory to show the emergence of vortices in conventional superconductors. With techniques from effective field theory such as Hubbard-Stratonovich transformation, we can derive the Ginzburg-Landau free energy from the microscopic BCS theory<sup>[26]</sup>, but we will not dive into the derivation in our article. Here we just straightly write down the famous Ginzburg-Landau theory :

$$F = \int f_s d^3x = \int_{\mathbf{x}} \left( \alpha |\Psi|^2 + \frac{\beta}{2} |\Psi|^4 + \frac{1}{2m^*} \left| \left( -i\hbar \nabla - \frac{e^*}{c} A \right) \Psi \right|^2 + \frac{B^2}{8\pi} \right) \quad (2.18)$$

where  $f_s$  is the free energy of superconducting states and  $f_n$  is the free energy of normal states. Note that in Eq. (2.18) we have used  $\Psi$  to denote the order parameter  $\Delta$  to be consistent with traditional notation which is widely used , different from the notation system in the previous subsection. Besides, we have some quantitative relations between those parameters in Eq. (2.18)

$$\alpha = \alpha' \frac{T - T_c}{T_c}, \beta = \frac{\alpha'}{N_e}, e^* = 2e, m^* = 2m \quad (2.19)$$

where  $\alpha'$  is a constant proportional to the square of critical temperature  $T_c$ . Furthermore, we define two new parameter to facilitate our discussion. One of them is the magnetic penetration depth  $\lambda_s = \sqrt{\frac{m^* c^2}{4\pi N_e e^{*2}}}$ , which can be measured from experiments. The other is the coherence length  $\xi = \sqrt{\frac{\hbar^2}{2m^* |\alpha'|}}$ , this quantity, to some extent, can be thought as the penetration length of the normal states into the superconductors. Ginzburg-Landau parameter is defined to be  $\kappa = \lambda_s/\xi$ .

As is known to all, there are mainly two types of superconductors. Type 1 and Type 2 superconductors differ fundamentally in their response to magnetic fields. Type 1 superconductors, typically pure metals like lead and mercury, exhibit perfect diamagnetism (complete Meissner effect) below a single critical field  $H_c$ , where they abruptly transition to the normal state. They are characterized by  $\kappa < \frac{1}{\sqrt{2}}$ , meaning their magnetic penetration depth is smaller than their coherence length. In contrast, Type 2 superconductors, including most high-Tc materials , have  $\kappa > 1/2$ , allowing magnetic flux to penetrate as quantized vortices between lower ( $H_{c1}$ ) and upper ( $H_{c2}$ ) critical fields. This creates a mixed state where superconductivity persists in higher fields, making Type 2 superconductors technologically valuable for applications requiring strong magnetic fields. In the following, we will show why vortices emerge in Type 2 superconductors.

The useful tool we use to classify the type of superconductors is the systems' surface energy density  $\sigma_s$ . When the surface energy of the systems is positive, we assert that the interface area of normal states and superconducting states is inclined to be enlarged. Therefore, numerous vortices with quantized magnetic flux will emerge within the Type 2 superconductor. On the contrary, the Type 1 superconductors are characterized by their negative surface energy. The phase in a Type 1 superconductor tends to be uniform; thus, it will be diamagnetic. We can calculate the Gibbs free energy of the superconductor and metal coexisting with a uniform magnetic field strength  $H_c$ , and let the surface energy to be the difference of this energy and the Gibbs free energy which is obtained based on Eq. (2.18). The surface energy can be expressed

as (the surface is set to be y-z plane)

$$\sigma_s = \int d^3\mathbf{x} \quad \alpha |\Psi|^2 + \frac{\beta}{2} |\Psi|^4 + \frac{1}{2m^*} \left| \left( -i\hbar\nabla - \frac{e^*}{c} A \right) \Psi \right|^2 + \frac{(B - H_c)^2}{8\pi} \quad (2.20)$$

, based on the fact that the uniform Gibbs energy density is  $-\frac{H_c^2}{8\pi}$ . Notice the properties of systems that the order parameter is zero at region  $x \rightarrow +\infty$  (metal) while in a superconductor the order parameter is  $\Psi = \Psi_0(x \rightarrow -\infty)$  and the magnetic induction intensity  $B = 0$  for  $x \rightarrow -\infty$  (superconductor) region. Since the system is in equilibrium, we have

$$\frac{\delta\sigma_s}{\delta A} = 0, \frac{\delta\sigma_s}{\delta\Psi} = 0 \quad (2.21)$$

To further simplify the expression of surface energy, we integrate by parts, arriving at the conclusion that<sup>[27]</sup>:

$$\sigma_s = \frac{H_c^2}{8\pi} \int_{\infty} dx \left[ \left( \frac{B(x)}{H_c} - 1 \right)^2 - \left( \frac{\Psi(x)}{\Psi_0} \right)^2 \right] \quad (2.22)$$

where  $\Psi_0 = \sqrt{-\frac{\alpha}{\beta}}$  is the value of  $\Psi$  corresponding to the minimum of free energy F. We go on with the assumption: in Type 1 superconductor,  $B = H_c\Theta(x)$  while the magnetic field is not uniform anymore in Type 2 superconductor but we guess  $\Psi = \Psi_0\Theta(-x)$ . From which we deduce that

$$\frac{\sigma_s}{A} = \frac{H_c^2}{8\pi} \times \begin{cases} 1.89\xi & \text{Typical Type 1 Superconductor} \\ -1.10\lambda_s & \text{Typical Type 2 Superconductor} \end{cases} \quad (2.23)$$

The critical point of the phase transition happens at  $\sigma_s = 0$ , hence through calculation we can find the critical point is  $\kappa = \frac{1}{\sqrt{2}}$ . Only when  $\kappa > \frac{1}{\sqrt{2}}$ , the superconductor belongs to the type 2 superconductors.

## 2.2 BKT Phase Transition

As is discussed above, conventional superconductors can be described by the Ginzburg-Landau theory, in this frame of theory, the superconductor-metal quantum phase transition aligns well with Landau's theory of second order phase transition. This sort of second order phase transition is characterized by the spontaneous breaking of continuous symmetry, related to the Goldstone modes. In the Ginzburg-Landau theory of superconductors, there is a global U(1) gauge symmetry of the phase of the order parameter,  $\Psi = |\Psi| e^{i\phi}$ , if the gauge field (gauge potential) A is zero. This is actually the case in the superfluid, which hosts no charge compared with superconductors. According to the Goldstone's theorem, there will be a gapless(soft)

Goldstone mode in systems with spontaneous symmetry breaking. However, in Ginzburg-Landau theory of superconductors, things become different—the gauge field  $\mathbf{A}$  has a profound impact on the physics of superconductors. The coupling between the gauge field  $\mathbf{A}$  and the Goldstone mode  $\phi$  leads to the so-called Anderson-Higgs mechanism, deducing the global  $U(1)$  to the local  $U(1)$  gauge symmetry. Anderson-Higgs mechanism tells us such a fact: the gauge field  $\mathbf{A}$  acquires its mass for the coupling to the gapless Goldstone mode  $\phi$ . This fact can be seen through the London equations, which are the first successful phenomenology of superconductivity:

$$\mathbf{j} = \frac{mc}{N_s e^2} \mathbf{A} \quad (2.24)$$

, and the mass term can also be seen explicitly in the Maxwell's equations  $(\nabla^2 - \frac{\rho_0}{m})\mathbf{B} = 0$ .

However, the Landau's theory of phase transitions fails in the systems with dimension( $D$ ) lower than 2. The foundation of this theory is spontaneous symmetry breaking, while the mechanism is "forbidden" in dimensions  $D \leq 2$ . We have a "no-go" theorem, the powerful Mermin-Wagner theorem<sup>[28][29]</sup>, stating that 2D systems and 1D systems with a continuous symmetry cannot be long-range ordered, i.e. will preserve the symmetry if there are no external forces. This theorem can be proved by showing the fluctuation in 2D systems and 1D systems will make the fluctuation of Goldstone modes diverge, thus the breaking symmetry will be repaired. The Mermin-Wagner theorem applies to a lot of systems, for instance, magnetic systems (Goldstone mode:magnon), solids (phonon) and superfluid (Goldstone mode: phases of the order parameters). The long range orders will be destroyed according to this no-go theorem. Although the classical-quantum mapping tells us the field theory of a dimensional quantum system can be mapped into a field theory of a  $(d+1)$  dimensional classical systems by adding a term in the form  $\psi \partial_\tau \psi$ , in which variable  $\tau$  denotes the dimension of temperature—the imaginary time, we claim that finite temperature 2D quantum systems are equivalent to corresponding thick 2D classical systems. In this way, the Mermin-Wagner theorem is still valid for finite temperature 2D superconductors.

It is a fact that universally acknowledged that experimentalists have observed quantum phase transitions in system whose dimension  $D \leq 2$ , so why do the experimental results contradict theoretical prediction of Mermin-Wagner theorem? As a matter of fact, Mermin-Wagner theorem still holds and the experimentalists are also correct. What really happened is the failure of Landau's theory. The quantum phase transitions of 2D superconducting states to normal states should be included in the frame of topological quantum phase transitions instead of spontaneous symmetry breaking. Physicists turned their eyes on topological excitations-vortices in

superconductors, and came up with the theory of BKT phase transition. The rest of this section is organized as following: first we will introduce the classical two-dimensional XY model to illustrate the low energy physics of 2D superconductors and superfluid, then we will derive some useful results and find the critical point of the BKT phase transition through rough discussion, finally we will show the voltage-current relation near the quantum critical point, which can be seen later in chapter 四 as an experimental fact.

### 2.2.1 2D Classical XY Model

Classical 2D XY model captures the low energy physics of superfluid<sup>[30]</sup>, but this model was first used in the research of classical magnetic systems. In this model, we have a SO(2) symmetry of spin direction and a square lattice to place the spinful atoms. The spin at site  $i$  of the square lattice is denoted by its direction  $\phi_i$ , ( $S_{i,x} - iS_{i,y} = \Psi_0 e^{i\phi_i}$ ) and the Hamiltonian can be written as:

$$H = -\kappa \sum_{\langle i,j \rangle} \cos(\phi_i - \phi_j) \approx E_0 + \frac{\kappa}{2} \int d^2x (\nabla \phi(\mathbf{r}))^2 \quad (2.25)$$

We only keep the hopping between the nearest neighbor and assume that the direction  $\phi$  varies slowly in space. Note that the spin direction  $\phi$  can also be thought as the phase of the order parameter and SO(2) is equivalent to the U(1) gauge symmetry. Since people are interested in the correlation function of order parameters, we need to calculate

$$\langle \Psi^*(\mathbf{r}) \Psi(0) \rangle = |\Psi_0|^2 \langle e^{i\phi(\mathbf{r})} e^{i\phi(0)} \rangle = |\Psi_0|^2 e^{-\frac{1}{2} \langle (\phi(\mathbf{r}) - \phi(0))^2 \rangle} \quad (2.26)$$

In the last step of Eq. (2.26) we have used the nontrivial property of Gaussian action Eq. (2.25), i.e.  $\langle e^{iX} \rangle = e^{-\frac{1}{2}\sigma^2}$  where  $X$  is the Gaussian variable and  $\sigma$  is the variance in Gaussian distribution. The variance is easy to calculate:

$$\langle (\phi(\mathbf{r}) - \phi(0))^2 \rangle = \int \int \frac{d^2\mathbf{k}}{(2\pi)^2} \frac{d^2\mathbf{k}'}{(2\pi)^2} (e^{i\mathbf{k} \cdot \mathbf{r}} - 1)(e^{i\mathbf{k}' \cdot \mathbf{r}} - 1) \langle \phi_{\mathbf{k}} \phi_{\mathbf{k}'} \rangle \quad (2.27)$$

From the expression of Hamiltonian we obtain that (let  $k_B = \hbar = c = 1$ )

$$\langle \phi_{\mathbf{k}} \phi_{\mathbf{k}'} \rangle = \delta(\mathbf{k} + \mathbf{k}') \frac{T}{\kappa} \frac{1}{k^2} \quad (2.28)$$

Thus now we have

$$\langle (\phi(\mathbf{r}) - \phi(0))^2 \rangle = \frac{T}{\kappa} \int \frac{d^2\mathbf{k}}{(2\pi)^2} 2(1 - \cos(\mathbf{k} \cdot \mathbf{r})) \frac{1}{k^2} \quad (2.29)$$

We focus on the long range behavior of the correlation function and we give the integral in Eq. (2.29) an ultraviolet cutoff  $1/\xi$ . Finally, we find that the correlation function of order

parameters is

$$\langle \Psi^*(\mathbf{r})\Psi(0) \rangle = |\Psi_0|^2 \left(\frac{\xi}{r}\right)^\eta, \quad \eta = \frac{T}{2\pi\kappa} \quad (2.30)$$

Eq. (2.30) indicates that the order parameters in the 2D classical XY model can be quasi long-range ordered when the effect of vortices can be neglected, aligning with the statement of Mermin-Wagner theorem.

### 2.2.2 Vortices in XY Model

In the previous subsection we dive into the physics of ordered states in 2D XY model. In this subsection, we will show how to characterize a quantum phase transition without spontaneous symmetry breaking. Vortices belong to the family of topological defects and also can be called "topological excitation". Obviously, the appearance of vortices breaks no symmetry so we can construct a theory of quantum phase transitions beyond the old Landau's theory. Since the phase  $\phi$  is single-valued, it must satisfy

$$\oint \nabla\phi(\mathbf{r}) \cdot d\mathbf{r} = 2\pi n, \quad n \in \mathbb{Z} \quad (2.31)$$

and  $n$  counts the number of winding. A commonly used solution of Eq. (2.31) is

$$\phi(x, y) = n \arctan \left( \frac{y - y_0}{x - x_0} \right) \quad (2.32)$$

which describes a vortex located in the position  $(x_0, y_0)$ . And the energy of a single vortex with radius  $\xi$  is given by:

$$E = E_{core} + n^2 \frac{\kappa}{2} \int_\xi^L (\nabla\phi)^2 = E_{core} + n^2 \pi \kappa \ln \left( \frac{L}{\xi} \right) \quad (2.33)$$

,in which  $\xi$  is the radius of the vortex,  $L$  is the size of the system and  $E_{core}$  is the energy for  $r < \xi$ . It is straightforward to figure out that this energy is divergent when  $L$  is sufficiently large. However, we can add another "antivortex" characterized by an opposite winding number  $-n$  to neutralize the divergent energy. The energy of this vortex-antivortex pair is :

$$E_{pair} = 2\pi\kappa n^2 \ln \left( \frac{x_0}{\xi} \right) + Const \quad (2.34)$$

and  $x_0$  is the distance between the two vortices. So, all we need to do now is to find the critical temperature  $T_{KT}$ , below which the systems do not have the inclination to create a vortex and the free energy cost of creating a single vortex is positive. We follow the Kosterlitz-Thouless argument<sup>[31]</sup>, assuming that the possibility to create a vortex is:

$$P = \left( \frac{L}{\xi} \right)^2 \exp \left( \frac{E_{core}}{T} - \frac{\pi\kappa}{T} \ln \left( \frac{L}{\xi} \right) \right) \quad (2.35)$$

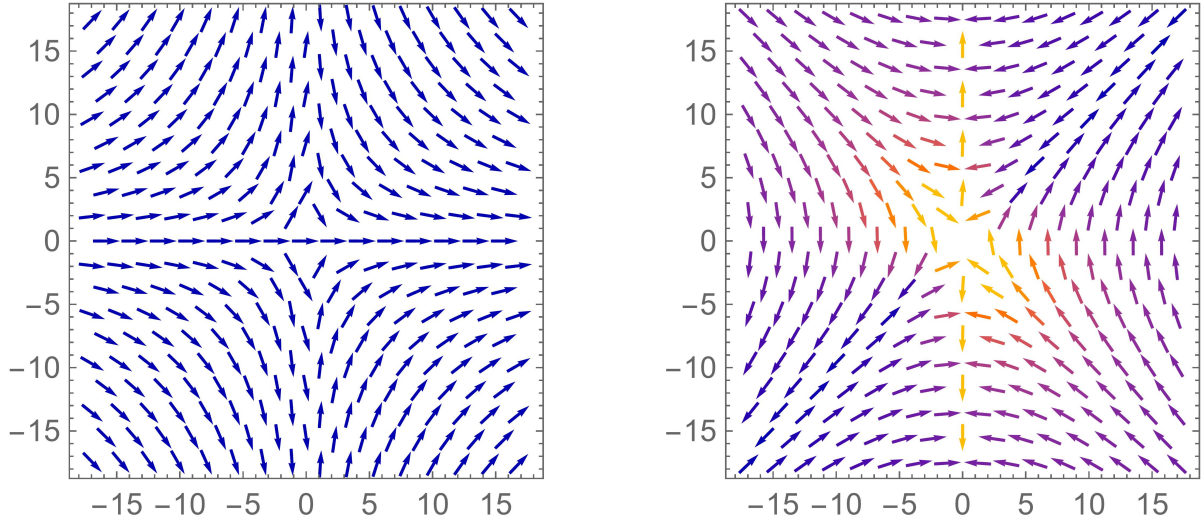


图 2.1 The left subfigure plots the spin configuration  $S_x - iS_y = e^{i\phi}$  of a single vortex with winding number 1 located in  $(0,0)$ . The right subfigure is the spin configuration where there are one vortex (winding number  $n=1$ ) at  $(1,1)$  and an antivortex at  $(-1,-1)$ .

The  $(\frac{L}{\xi})^2$  term stems from the approximation that we have  $(L/\xi)^2$  positions to locate the vortex. When the ratio of system size to the radius of vortex is sufficiently large, we can drop the  $E_{core}$ . Thus the critical temperature is

$$T_{KT} = \frac{\pi K}{2} \quad (2.36)$$

which is consistent with the  $F = E - TS$  evidence.

With all the previous discussion, we are able to figure out the physics behind BKT phase transition. The BKT phase transition is a topological phase transition driven by the binding and unbinding of vortex-antivortex pairs. In the low-temperature phase ( $T < T_{KT}$ ), these topological defects remain tightly bound due to logarithmic interaction potentials, preserving quasi-long-range order characterized by power law decay of correlation functions,  $\langle \Psi^*(\mathbf{r})\Psi(0) \rangle = |\Psi_0|^2 (\frac{\xi}{r})^\eta$ . This phase supports superconductivity in 2D systems, as bound vortices do not disrupt global phase coherence, allowing persistent currents without dissipation. Above the critical temperature ( $T > T_{KT}$ ), thermal fluctuations overcome the binding energy, liberating free vortices that proliferate and destroy long-range phase coherence, leading to exponential decay of correlations and the emergence of finite resistivity. In 2D superconductors, the BKT transition explains the sharp drop in resistance near  $T_{KT}$ , where vortex-antivortex pair dissociation triggers the loss of superconductivity. Unlike conventional superconductors, where Cooper pair condensation dominates, 2D superconductivity is governed by phase fluctuations and vortex dynamics, making the BKT framework essential for understanding thin films, interfaces, and layered materials where dimensionality suppresses long-range order but allows topological

defects to dictate critical behavior.

### 2.2.3 Voltage-Current Relation Near the Critical Point

In the last part of this chapter, we will briefly discuss the voltage-current relation near the critical temperature  $T_{KT}$ . The Lorentz force will bring an additional term in the potential of vortex-antivortex pairs. We will consider the basic bound state: vortex-antivortex pair with winding number 1(-1). Then the energy of a pair can be written down as:

$$U(x_0) = 2\pi\kappa \ln\left(\frac{x_0}{\xi}\right) - \frac{Ix_0\Phi_0}{cA} \quad (2.37)$$

where  $\Phi_0 = \frac{h}{2e}$  and A is the conduction area of the current. Using  $\frac{\partial U(x_0)}{\partial x_0} = 0$ , we find the extreme value of the energy is

$$U_{max} = 2\pi\kappa \ln\left(\frac{2\pi\kappa cA}{I\Phi_0\xi}\right) - 2\pi\kappa = 2\pi\kappa \left( \ln\left(\frac{I_0}{I}\right) - 1 \right) \quad (2.38)$$

and the parameter  $I_0 = \frac{2\pi\kappa cA}{\Phi_0\xi}$ . For the number of free vortices  $N$ , we have

$$\frac{dN}{dt} = \Gamma(T) - AN^2 \quad (2.39)$$

where  $\Gamma$  is the decoupling rate of the vortex-antivortex pairs and A is the coefficient of rebounding rate. We assume that the decoupling rate takes the form  $\Gamma \approx B \exp(-U_{max}/T)$ , therefore the steady number of free vortices is:

$$N = \sqrt{\frac{B}{A}} \exp(-U_{max}/(2T)) \quad (2.40)$$

Because every free vortex is approximately independent in our calculation, the resistivity of our systems is supposed to be proportional to  $N^{[32]}$ , so the voltage V is

$$V = IR \propto NI = \sqrt{\frac{B}{A}} e^{\frac{\pi\kappa}{T}} I_0 \left(\frac{I}{I_0}\right)^{\frac{\pi\kappa}{T}+1} \quad (2.41)$$

When the temperature is close to the critical temperature  $T_{KT} = \pi\kappa/2$ , the voltage-current relation is  $V \propto I^3$ , which can be observed in the experiment of 2D superconductor.



## 第三章 Constructing Continuum Models

The electronic behavior of twisted bilayer materials, such as transition metal dichalcogenides (TMDs), is governed by the delicate interplay between atomic stacking, interlayer hybridization, and the emergent structure of moiré superlattice. This chapter outlines a systematic approach to constructing continuum models out of density functional theory(DFT) results that capture the low-energy physics of these systems, emphasizing the role of symmetry, stacking configurations, and first-principles insights. By bridging atomic-scale details with effective theories, we establish a framework to describe topological bands and correlated phases in twisted bilayer TMDs, such as  $\text{MoTe}_2$  and  $\text{WSe}_2$ , without relying on empirical parameter fitting<sup>[33][34]</sup>.

We begin by contrasting two fundamental stacking configurations: AA stacking, where atoms align vertically between layers, and AB stacking, characterized by a  $180^\circ$  rotation that creates alternating registries. In twisted bilayers, the relative rotation between layers generates different moiré patterns—a long-range periodic modulation of atomic alignment. For commensurate twist angles, this pattern exhibits exact translational symmetry, enabling the classification of electronic states by moiré momentum. The emergence of this symmetry is tied to the geometric condition where the twist angle forms a "magic" ratio between the lattice constants of the two layers, creating a supercell that repeats seamlessly across the material. Furthermore, even for incommensurate angles, one can also construct an appropriate continuum model if this angle is sufficiently small or near a commensurate angle<sup>[35]</sup>.

The low-energy electronic structure is further shaped by valley-specific physics. For example, in  $\text{MoTe}_2$ , electrons near the K valleys inherit strong spin-orbit coupling and layer-dependent phase factors, while the  $\Gamma$  valley hosts flatter bands<sup>[36][37]</sup>. On the contrary, in twisted bilayer graphene (TBG), only the low energy physics in monolayer graphene near K point, the Dirac point, contributes to the low energy of TBG that we are primarily concerned with. To model these effects, we derive effective Hamiltonians using symmetry-guided expansions. Under many circumstances, first-harmonic terms capture the dominant moiré potential, however, higher-order corrections are essential to reproduce subtle features. As a result, one aims to search for a useful method to include as many effective parameters as possible , so that the model can fit the ab-initio results better.

A key advancement in our approach lies in the ab-initio determination of model param-

eters. Instead of relying on empirical fitting, we extract critical quantities—such as effective masses, interlayer couplings, and intralayer moiré potentials—directly from density functional theory (DFT) calculations. This methodology ensures parameter transferability across twist angles and stacking geometries, bypassing ambiguities inherent in traditional fitting procedures. By unifying crystalline symmetry constraints, moiré periodicity, and first-principles inputs, this framework provides a predictive tool for engineering topological and correlated states in twisted TMDs. It establishes a direct pathway from atomic structure to emergent quantum phenomena, offering insights into the design of tailored electronic systems with precise control.

### 3.1 Stacking Configurations and Interlayer Hopping

In this section, we will discuss the method based on two center approximation to derive the effective continuum model of twisted materials. We will firstly show the derivation of interlayer hopping Hamiltonian of  $K$  valley in AA stacking configuration. To facilitate the discussion of WSe<sub>2</sub> later in the article, we attach emphasis on the case of honeycomb lattice, which preserves the  $C_{3z}$  rotational symmetry. The next step is to study the AB stacking interlayer Hamiltonian, slightly different from the AA stacking case but the methods are highly similar. The methods discussed in this section also works in deriving the continuum model which stems from the  $\Gamma$  and  $M$  valley, illuminating the ways to derive effective model of different valleys<sup>[33]</sup>.

#### 3.1.1 AA Stacking

In this section we will build a model following the way shown in the bibliography<sup>[5]</sup>.  $l=1(-1)$  is the layer index,  $\hat{a}_{\mathbf{R},s,l}^\dagger$  creates a Wannier orbital with index  $s$  of the lowest conduction band at  $\mathcal{R}_{\theta,l}\mathbf{R}$  in layer  $l$ . Fourier transformation takes the form :

$$\hat{a}_{\mathbf{k},s,l}^\dagger = \frac{1}{\sqrt{N}} \sum_{\mathbf{R}} \hat{a}_{\mathbf{R},s,l}^\dagger e^{i\mathbf{k} \cdot (\mathcal{R}_{\theta,l}\mathbf{R} + d_l)} \quad (3.1)$$

$R_{\theta,l}$  denotes the rotation matrix of layer  $l$ ,  $d_l$  is the translation due to incommensurate structure. Because  $d_l$  finally can be gauged away in the case of small angle, we can simply neglect it in our derivation for simplicity. The interlayer hopping matrix of AA stacking materials is defined as

$$[h_{AA}^{bl}(\mathbf{k}, \mathbf{k}')]_{s_1 l_1; s_2 l_2} = \langle \mathbf{k}, s_1, l_1 | H_{AA} | \mathbf{k}', s_2, l_2 \rangle \quad (3.2)$$

We make an assumption that the magnitude of interlayer hopping only relies on the distance  $\mathbf{R} - \mathbf{R}'$ , thus we have

$$[h_{\text{AA}}^{\text{bl}}(\mathbf{k}, \mathbf{k}')]_{s_1 l; s_2 (-l)} = \frac{1}{N} \sum_{\mathbf{R}, \mathbf{R}'} e^{i\mathbf{k}' \cdot \mathcal{R}_{\theta, -l} \mathbf{R}'} e^{-i\mathbf{k} \cdot \mathcal{R}_{\theta, l} \mathbf{R}} \langle \mathbf{R}, s_1, l | H_{\text{AA}} | \mathbf{R}', s_2, -l \rangle \quad (3.3)$$

$$\langle \mathbf{R}, s_1, l | H_{\text{AA}} | \mathbf{R}', s_2, -l \rangle = t_{s_1 s_2}^{\text{AA}} (R_{\theta, l} \mathbf{R} - R_{\theta, -l} \mathbf{R}') \quad (3.4)$$

And we can express the magnitude  $t(\mathbf{R})$  as :

$$t_{s_1 s_2}^{\text{AA}} (\mathcal{R}_{\theta, l} \mathbf{R} - \mathcal{R}_{\theta, -l} \mathbf{R}') = \frac{1}{N \Omega_{\text{tot}}} \sum_{\mathbf{q} \in \text{1BZ}, \mathbf{G}} t_{s_1 s_2}^{\text{AA}} (\mathbf{q} + \mathbf{G}) e^{i(\mathbf{q} + \mathbf{G})(\mathcal{R}_{\theta, l} \mathbf{R} - \mathcal{R}_{\theta, -l} \mathbf{R}')} \quad (3.5)$$

This is the two center approximation. 1BZ is the Brillouin Zone for the monolayer unrotated material,  $\mathbf{G}$  represents the reciprocal lattice vectors. Applying Fourier transformation, we get:

$$\begin{aligned} [h_{\text{AA}}^{\text{bl}}(\mathbf{k}, \mathbf{k}')]_{s_1 l; s_2 (-l)} &= \sum_{\substack{\mathbf{q}, \mathbf{G} \\ \mathbf{G}', \mathbf{G}''}} \frac{t_{s_1 s_2}^{\text{AA}}(\mathbf{q} + \mathbf{G})}{\Omega_{\text{tot}}} \delta_{\mathbf{q} + \mathbf{G} - \mathbf{k}', \mathcal{R}_{\theta, -l} \mathbf{G}'} \delta_{\mathbf{k} - \mathbf{q} - \mathbf{G}, \mathcal{R}_{\theta, l} \mathbf{G}''} \\ &= \sum_{\mathbf{G}', \mathbf{G}''} \frac{t_{s_1 s_2}^{\text{AA}}(\mathbf{k}' + \mathcal{R}_{\theta, -l} \mathbf{G}')}{\Omega_{\text{tot}}} \delta_{\mathbf{k} - \mathbf{k}', \mathcal{R}_{\theta, l} \mathbf{G}'' + \mathcal{R}_{\theta, -l} \mathbf{G}'}, \end{aligned} \quad (3.6)$$

We are "rigorous" except for the two center approximation so far. According to the experiments, the magnitude of interlayer hopping  $t$  decays rapidly in the momentum space. The reason for the spike behavior is that the magnitude  $t(\mathbf{R})$  varies slowly in the real space because the interlayer distance is much larger than the normal length of effective intralayer distance  $\mathcal{R}_{\theta, l} \mathbf{R} - \mathcal{R}_{\theta, -l} \mathbf{R}'$ .

When the states originating from the  $K(K')$  valley dominate in the low energy physics, we suppose that  $\mathbf{k}$  can be expanded near the  $K$  valley. The widely used first harmonic oscillation assumes that only three kinds of hopping terms contribute to the interlayer Hamiltonian, corresponding to three equivalent  $K$  point, satisfying:

$$|\mathbf{k}' + R_{\theta, -l} \mathbf{G}'| \approx |K| \quad (3.7)$$

We can expand  $\mathbf{k}'$  and  $\mathbf{k}$  near  $K$  valley  $K' = \mathcal{R}_{\theta, l} K$ , where  $\delta\mathbf{k}$ ,  $\delta\mathbf{k}'$  is relatively small.

$$\mathbf{k} = \delta\mathbf{k} + K \quad (3.8)$$

$$\mathbf{k}' = \delta\mathbf{k}' + K' \quad (3.9)$$

Therefore, in the calculation of the module of  $\mathbf{k}' + \mathcal{R}_{\theta, -l} \mathbf{G}'$ , we can neglect  $\delta\mathbf{k}'$ . In this way, considering the constraint of Eq. (3.7), we conclude that:

$$\mathbf{G}' \in \{0, C_{3z} K - K, C_{3z}^2 K - K\} \quad (3.10)$$

Finally, Since the magnitude of  $\mathbf{k} - \mathbf{k}'$  is small compared with  $|K|$ , the relation  $\delta_{\mathbf{k}-\mathbf{k}', R_{\theta,l}\mathbf{G}'' - R_{\theta,-l}\mathbf{G}'} \neq 0$  only stands when  $\mathbf{G}'$  equals to  $\mathbf{G}$ . Define  $\mathbf{q}_j = C_{3z}^{j-1}(R_{\theta,l}\mathbf{G}' - R_{\theta,-l}\mathbf{G}')$ , Hamiltonian takes the form people are familiar with

$$[h_{AA}^{\text{bl}}(\mathbf{k}, \mathbf{k}')]_{s_1 l; s_2 (-l)} = \sum_{j=1}^3 \delta_{\mathbf{k}-\mathbf{k}', \mathbf{q}_j} T^j \quad (3.11)$$

### 3.1.2 AB Stacking

The difference between these two stacking configurations is characterized by the additional  $180^\circ$  rotation of the system. Therefore, the Fourier transformation of creation operators is different from AA stacking case:

$$\hat{a}_{\mathbf{k}, s, l}^\dagger = \frac{1}{\sqrt{N}} \sum_{\mathbf{R}} \hat{a}_{\mathbf{R}, s, l}^\dagger e^{il\mathbf{k} \cdot \mathcal{R}_{\theta,l}\mathbf{R}} \quad (3.12)$$

Note that there is a extra factor  $l$  indicating the bottom layer ( $l=-1$ ) rotates an additional  $180^\circ$ . With this definition, we are able to write down the interlayer hopping terms pf AB stacking Hamiltonian:

$$[h_{AB}^{\text{bl}}(\mathbf{k}, \mathbf{k}')]_{s_1 l; s_2 l_2} = \langle \mathbf{k}, s_1, l | H_{AB} | \mathbf{k}', s_2, l_2 \rangle \quad (3.13)$$

and all the notations are consistent with the previous subsection. Again, applying Fourier transformation:

$$[h_{AB}^{\text{bl}}(\mathbf{k}, \mathbf{k}')]_{s_1 l; s_2 (-l)} = \frac{1}{N} \sum_{\mathbf{R}, \mathbf{R}'} e^{-il\mathbf{k}' \cdot \mathcal{R}_{\theta,-l}\mathbf{R}'} e^{-il\mathbf{k} \cdot \mathcal{R}_{\theta,l}\mathbf{R}} \langle \mathbf{R}, s_1, l | H_{AB} | \mathbf{R}', s_2, -l \rangle \quad (3.14)$$

in which the expressions of the matrix elements can be simplified using the two center approximation:

$$\langle \mathbf{R}, s_1, l | H_{AB} | \mathbf{R}', s_2, -l \rangle = t_{s_1 s_2}^{\text{AB}} (-l\mathcal{R}_{\theta,-l}\mathbf{R}' - l\mathcal{R}_{\theta,l}\mathbf{R}) \quad (3.15)$$

$$= \frac{1}{N\Omega_{tot}} \sum_{\mathbf{q}, \mathbf{G}} t_{s_1 s_2}^{\text{AB}} (\mathbf{q} + \mathbf{G}) e^{i(\mathbf{q} + \mathbf{G}) \cdot (l\mathcal{R}_{\theta,-l}\mathbf{R}' + l\mathcal{R}_{\theta,l}\mathbf{R})}. \quad (3.16)$$

leading to the simplified expression of interlayer hopping:

$$\begin{aligned} [h_{AB}^{\text{bl}}(\mathbf{k}, \mathbf{k}')]_{s_1 l; s_2 (-l)} &= \sum_{\substack{\mathbf{q}, \mathbf{G} \\ \mathbf{G}', \mathbf{G}''}} \frac{t_{s_1 s_2}^{\text{AB}} (\mathbf{q} + \mathbf{G})}{\Omega_{tot}} \delta_{\mathbf{q} + \mathbf{G} - \mathbf{k}', -l\mathcal{R}_{\theta,-l}\mathbf{G}'} \delta_{\mathbf{k} - \mathbf{q} - \mathbf{G}, l\mathcal{R}_{\theta,l}\mathbf{G}''} \\ &= \sum_{\mathbf{G}', \mathbf{G}''} \frac{t_{s_1 s_2}^{\text{AB}} (\mathbf{k}' - l\mathcal{R}_{\theta,-l}\mathbf{G}')}{\Omega_{tot}} \delta_{\mathbf{k} - \mathbf{k}', l\mathcal{R}_{\theta,l}\mathbf{G}'' - l\mathcal{R}_{\theta,-l}\mathbf{G}'} \end{aligned} \quad (3.17)$$

This time we define  $K' = l\mathcal{R}_{\theta,l}K$ , then things just behave the same as AA stacking case.

### 3.2 General Method to Obtain Continuum Model

In the previous section, we have discussed the form of the off-diagonal part of Hamiltonian, describing the interlayer hopping terms. Though our derivation mainly focuses on the low energy physics of  $K$  valley, the procedure can also apply to more general cases. In this section, we will loosen the constraint put by the two center approximation, instead giving a more general form of the continuum model containing higher order terms and even gradient terms. Our goal is to provide a concise introduction to the method to obtain a continuum model from ab-initio calculation (DFT data) without parameter fitting, since the continuum obtained in this way is used in our Hartree Fock self-consistent calculation, which will be discussed later in this article.

To better address the general question, we need to have a more comprehensive viewpoint of the two center approximation. The well-known first harmonic two center approximation only holds when the higher order harmonic terms can be neglected, which is not the case in many members of the TMDs family. For example, the continuum model of  $\text{MoTe}_2$  (or  $\text{WSe}_2$ ) is supposed to include the second harmonic terms in the intralayer terms<sup>[38]</sup>. Moreover, the emergent symmetry of the continuum model may change according to the chosen approximation. For instance, we are interested in the superconductivity of  $3.89^\circ$  twisted bilayer  $\text{WSe}_2$ , whose twist angle is incommensurate. The incommensurate heterostructure should preserve fewer exact symmetries, then one may ask: "why does the obtained continuum model still inherit so many kinds of symmetries from the monolayer materials?" The origin of those emergent symmetries is just the approximation. The two center approximation stands only when the starting position of the interlayer hopping makes no difference, thus we claim that the continuum model actually admits a commensurate geometry under two center approximation, even at an incommensurate twist angle. Besides, this hidden commensurate configuration may preserve additional symmetries due to further approximation like first harmonic approximation. Therefore, the emergent symmetry is, to some extent, the exact symmetry of the corresponding effective commensurate structure rising out of approximation.

This provides people with a new perspective to obtain the continuum model from ab-initio calculation. We can begin with symmetry analysis and get the symmetry constraint of our continuum models. In this way, people are able to figure out which kinds of interlayer and intralayer hopping terms exist in our continuum models. Fully aware of the expression of the target continuum model, one can obtain the values of parameters of the continuum models from the ab-initio calculation. The "automatic" fitting method will also be shown in this section.

### 3.2.1 Symmetry and Basic Notation

We use the following basis for the moiré unit cell:

$$\mathbf{a}_{M,1} = a_M \left( \frac{\sqrt{3}}{2}, -\frac{1}{2} \right), \quad \mathbf{a}_{M,2} = a_M (0, 1), \quad (3.18)$$

$$\mathbf{b}_{M,1} = \frac{4\pi}{\sqrt{3}a_M} (1, 0), \quad \mathbf{b}_{M,2} = \frac{4\pi}{\sqrt{3}a_M} \left( \frac{1}{2}, \frac{\sqrt{3}}{2} \right), \quad (3.19)$$

where  $a_M = a_0/2 \sin(\frac{\theta}{2})$  is the moiré unit cell lattice constants. We first consider the monolayer WSe<sub>2</sub>. At  $K$  valley, the top valence band is mainly given by the  $d_{x^2-y^2}, d_{xy}$  orbitals of W atom, and has spin-valley locking due to strong Spin orbital coupling, i.e., the top valence band at the  $K$  valley is spin up while the  $-K$  valley is spin down. From ab-initio calculation, the Wannier basis of the top valence band can be chosen as  $d_{x^2-y^2} + id_{xy}$  and we will drop the spin index for readability. This is actually a universal property of group-VI TMD monolayers, which MoTe<sub>2</sub> also satisfies<sup>[39]</sup>.

The explicit expressions of  $K^l$  as the  $K$  point of the  $l$  layer are:

$$K^l = \frac{4\pi}{3a_0} \left( \cos\left(\frac{\theta}{2}\right), \sin\left(\frac{\theta}{2}\right) \right)^T, \quad K^{-1} = \frac{4\pi}{3a_0} \left( \cos\left(\frac{\theta}{2}\right), -\sin\left(\frac{\theta}{2}\right) \right), \quad (3.20)$$

which means that each layer is rotated by  $l\frac{\theta}{2}$ . To simplify the expression of continuum model, we decide to use the creation operator of low energy physics instead of the origin creation operator  $\hat{a}_{\mathbf{k},s,l}^\dagger$ . We use  $c_{\eta,l,\mathbf{r}}^\dagger$  to denote the electron creation operator where  $\eta = \pm 1$  denotes the  $\pm K$  valley. The real space operation can be expressed via momentum-space operator as

$$\begin{aligned} c_{\eta,l,\mathbf{r}}^\dagger &= \frac{1}{\sqrt{\Omega_{tot}}} \sum_{\mathbf{k}} \sum_{\mathbf{Q} \in Q_l^\eta} e^{-i(\mathbf{k}-\mathbf{Q}) \cdot \mathbf{r}} c_{\eta,\mathbf{k},\mathbf{Q}}^\dagger \\ c_{\eta,\mathbf{k},\mathbf{Q}}^\dagger &= \frac{1}{\sqrt{\Omega_{tot}}} \int d^2 \mathbf{r} c_{\eta,l,\mathbf{r}}^\dagger e^{i(\mathbf{k}-\mathbf{Q}) \cdot \mathbf{r}}, \quad \mathbf{Q} \in Q_l^\eta \end{aligned} \quad (3.21)$$

where  $Q_l^\eta = \{\mathbf{G}_M + \eta(-1)^l \mathbf{q}_1 | \mathbf{G}_M \in \mathbb{Z}\mathbf{b}_{M,1} + \mathbb{Z}\mathbf{b}_{M,2}\}$ . Note that  $\mathbf{k}$  denotes the momentum measured from  $\eta K$  valley, different from the  $\mathbf{k}$  in  $\hat{a}_{\mathbf{k},s,l}^\dagger$ . In the rest of this article,  $X_M$  means quantity  $X$  in the moiré unit cell. Symmetry constraints of the WSe<sub>2</sub> with AA stacking configuration can be written down as follows:

$$C_3 c_{\eta,l,\mathbf{r}}^\dagger C_3^{-1} = c_{\eta,l,C_3 \mathbf{r}}^\dagger e^{i\eta\pi/3} \quad (3.22)$$

$$(C_{2y}\mathcal{T}) c_{\eta,l,\mathbf{r}}^\dagger (C_{2y}\mathcal{T})^{-1} = c_{\eta,\bar{l},C_{2y}\mathbf{r}}^\dagger \quad (3.23)$$

$$\mathcal{T} c_{\eta,l,\mathbf{r}}^\dagger \mathcal{T}^{-1} = c_{-\eta,l,\mathbf{r}}^\dagger (-\eta) \quad (3.24)$$

$$T_{\mathbf{R}_M} c_{\eta,l,\mathbf{r}}^\dagger T_{\mathbf{R}_M}^{-1} = c_{\eta,l,\mathbf{r}+\mathbf{R}_M}^\dagger e^{-i\eta\mathbf{R}_M \cdot \mathbf{K}_l} \quad (3.25)$$

where  $\mathcal{T}$  denotes the time reversal symmetry and  $T_{\mathbf{R}_M}$  is the moiré translational symmetry. Since the  $-K$  valley is the time reversal counterpart of the  $K$  valley, the Hamiltonian of  $-K$  valley is also the time reversal counterpart of the Hamiltonian of  $K$  valley. As a matter of fact, many of these symmetries are emergent symmetry in incommensurate twist angle. However, we can use some tricks to deduce the continuum model of incommensurate configurations from the established results of commensurate configurations, which is the case in our Hartree Fock calculation.

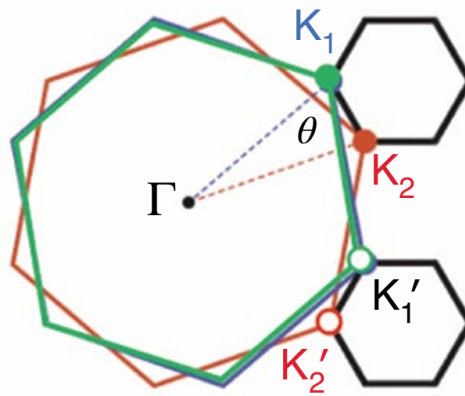


图 3.1 This picture is cited from literature<sup>[4]</sup>. The image clearly demonstrates the generation of moiré superlattice. The top(green) layer of graphene and bottom(red) layer of graphene are rotated by a twist angle  $\theta$ . We can observe in this picture that the moiré superlattice is still hexagonal.

### 3.2.2 Second Harmonic Model and General Expression

In tWSe<sub>2</sub>, the most general expression of the continuum models of AA-stacked Hamiltonian ( $K$  valley) reads:

$$\partial_z = \partial_x + i\partial_y, \quad \partial_{z^*} = \partial_x - i\partial_y, \quad (3.26)$$

$$H_K^{AA}(\mathbf{r}) = \sum_l \int d^2r \left[ c_{l,r}^\dagger \frac{\hbar^2 \nabla^2}{2m^*} c_{l,r} + \sum_{m_1 m_2 n_1 n_2 \in \mathbb{N}} \left( i^m \partial_z^{m_1} \partial_{z^*}^{m_2} c_{l,r}^\dagger \right) V_l^{m_1 m_2 n_1 n_2}(\mathbf{r}) (-i)^n \partial_z^{n_1} \partial_{z^*}^{n_2} c_{l,r} \right] \\ + \sum_{m_1 m_2 n_1 n_2 \in \mathbb{N}} \sum_l \int d^2r \left( i^m \partial_z^{m_1} \partial_{z^*}^{m_2} c_{l,r}^\dagger \right) w_{l-l}^{m_1 m_2 n_1 n_2}(\mathbf{r}) (-i)^n \partial_z^{n_1} \partial_{z^*}^{n_2} c_{-l,r} \quad (3.27)$$

in which we drop the valley index  $\eta$ . The first term in Eq. (3.27) is the quadratic kinetic energy of the valence band, unlike the linear dispersion of TBG. The second term describes the intralayer hopping while the third term describes the interlayer hopping. The next step is to reduce the number of unknown parameters in Eq. (3.27) based on symmetry analysis. The moiré translational symmetry requires that:

$$\begin{aligned} V_l^{m_1 m_2 n_1 n_2}(\mathbf{r}) &= \sum_{\mathbf{G}_M} e^{-i \mathbf{G}_M \cdot \mathbf{r}} V_{l, \mathbf{G}_M}^{m_1 m_2 n_1 n_2} \\ w_{l-l}^{m_1 m_2 n_1 n_2}(\mathbf{r}) &= \sum_{\mathbf{G}_M} e^{-i(\mathbf{q}_1 + \mathbf{G}_M) \cdot \mathbf{r}} w_{l-l, \mathbf{q}_1 + \mathbf{G}_M}^{m_1 m_2 n_1 n_2} \end{aligned} \quad (3.28)$$

which can be reduced to the first harmonic level if we restrict the interlayer components to satisfy  $|\mathbf{q}_1 + \mathbf{G}_M| = |\mathbf{q}|$ . Besides, we can express the Hamiltonian in momentum space as:

$$\begin{aligned} h_{K, \mathbf{Q}\mathbf{Q}'}^{AA}(\mathbf{k}) &= -\delta_{\mathbf{Q}\mathbf{Q}'} \frac{\hbar^2(\mathbf{k} - \mathbf{Q})^2}{2m*} \\ &+ \sum_l \sum_{m_1 m_2 n_1 n_2} \sum_{\mathbf{G}_M} \delta_{\mathbf{Q}, \mathbf{Q}' + \mathbf{G}_M} V_{l, \mathbf{G}_M}^{m_1 m_2 n_1 n_2} (k - Q)_z^{m_1} (k - Q)_{z*}^{m_2} (k - Q')_z^{n_1} (k - Q')_{z*}^{n_2} \\ &+ \sum_{m_1 m_2 n_1 n_2} \sum_{\mathbf{G}_M} \sum_l \delta_{\mathbf{Q}, \mathbf{Q}' + \mathbf{G}_M + \mathbf{q}_1} w_{l-l, \mathbf{G}_M}^{m_1 m_2 n_1 n_2} (k - Q)_z^{m_1} (k - Q)_{z*}^{m_2} (k - Q')_z^{n_1} (k - Q')_{z*}^{n_2} \end{aligned} \quad (3.29)$$

In this expression,  $(k - Q)_z = (\mathbf{k} - \mathbf{Q})_x + i(\mathbf{k} - \mathbf{Q})_y$ ,  $(k - Q)_{z*} = (\mathbf{k} - \mathbf{Q})_x - i(\mathbf{k} - \mathbf{Q})_y$ .

Moreover, the requirements of  $C_{3z}$  read

$$\begin{aligned} V_{l, \mathbf{G}_M}^{m_1 m_2 n_1 n_2} &= V_{l, C_3^{-1} \mathbf{G}_M}^{m_1 m_2 n_1 n_2} \\ w_{l-l, \mathbf{G}_M + \mathbf{q}_1}^{m_1 m_2 n_1 n_2} &= w_{l-l, C_3^{-1}(\mathbf{G}_M + \mathbf{q}_1)}^{m_1 m_2 n_1 n_2} \end{aligned} \quad (3.30)$$

and the requirements of  $C_{2y}\mathcal{T}$  read

$$\begin{aligned} V_{l, \mathbf{G}_M}^{m_1 m_2 n_1 n_2 *} &= (-)^{m_1 + m_2 + n_1 + n_2} V_{-l, -C_{2y} \mathbf{G}_M}^{m_2 m_1 n_2 n_1} \\ w_{l-l, \mathbf{G}_M + \mathbf{q}_1}^{m_1 m_2 n_1 n_2 *} &= (-)^{m_1 + m_2 + n_1 + n_2} w_{-l-l, -C_{2y}(\mathbf{G}_M + \mathbf{q}_1)}^{m_2 m_1 n_2 n_1} \end{aligned} \quad (3.31)$$

Note that Hermiticity of our Hamiltonian also give some constraints on those coefficients:

$$\begin{aligned} V_{l, \mathbf{G}_M}^{m_1 m_2 n_1 n_2 *} &= V_{l, -\mathbf{G}_M}^{n_2 n_1 m_2 m_1} \\ w_{l-l, \mathbf{G}_M + \mathbf{q}_1}^{m_1 m_2 n_1 n_2 *} &= w_{-l-l, -(\mathbf{G}_M + \mathbf{q}_1)}^{n_2 n_1 m_2 m_1} \end{aligned} \quad (3.32)$$

Collecting all these symmetry constraints, the cost of numerical calculation will be much smaller. The remainder of the task is to give a cutoff to the momentum  $\mathbf{Q}$  and the reciprocal vector  $\mathbf{G}$ . For instance, in literature<sup>[38]</sup>, people apply so called second harmonic approximation

without including gradient terms, then the continuum model is :

$$H = \sum_{\mathbf{k}, \mathbf{Q}, \mathbf{Q}'} h_{\mathbf{Q}, \mathbf{Q}'}^{\eta}(\mathbf{k}) c_{\eta, \mathbf{k}, \mathbf{Q}}^{\dagger} c_{\eta, \mathbf{k}, \mathbf{Q}'} \quad (3.33)$$

where

$$\begin{aligned} h_{\mathbf{Q}, \mathbf{Q}'}^{\eta}(\mathbf{k}) = & \left[ -\frac{\hbar^2}{2m^*}(\mathbf{k} - \mathbf{Q})^2 + \frac{\epsilon}{2}\eta(-1)^{\mathbf{Q}} \right] \delta_{\mathbf{QQ}'} \\ & + V \sum_{i=1,2,3} \left[ e^{-\eta(-1)^{\mathbf{Q}_i} \psi} \delta_{\mathbf{Q}+\mathbf{g}_i, \mathbf{Q}'} + e^{\eta(-1)^{\mathbf{Q}_i} \psi} \delta_{\mathbf{Q}-\mathbf{g}_i, \mathbf{Q}'} \right] \\ & + \sum_{i=1,2,3} [w \delta_{\mathbf{Q}+\mathbf{q}_i, \mathbf{Q}'} + \text{h.c.}] \end{aligned} \quad (3.34)$$

Notation  $(-)^{\mathbf{Q}}$  equals to  $\pm 1$  for  $\mathbf{Q} \in \{\mathbf{G}_M \pm \mathbf{q}_1\}$ . Vector  $\mathbf{g}_i = C_{3z}^{i-1} \mathbf{b}_{M,1}$ . The parameters are chosen to be<sup>[38]</sup>

$$a_0 = 3.317A^\circ \quad V = 9\text{meV} \quad w = -18.0\text{meV} \quad \psi = -128^\circ \quad (3.35)$$

and  $\epsilon$  denotes the displacement field. In the following chapter, we will compare the Hartree Fock phase diagrams generated by the second harmonic model with ones generated by the DFT model. To facilitate later discussion, We write down the notations of the eigenvalues and eigenvectors of single particle Hamiltonian as

$$h_{\mathbf{Q}, \mathbf{Q}'}^{\eta}(\mathbf{k}) U_{\mathbf{Q}, n}^{\eta}(\mathbf{k}) = \epsilon_{\mathbf{k}, n}^{\eta} U_{\mathbf{Q}, n}^{\eta}(\mathbf{k}) \quad (3.36)$$

Electron operators in the band basis are then

$$\gamma_{\mathbf{k}, n, \eta} = \sum_{\mathbf{Q}} U_{\mathbf{Q}, n}^{\eta, *}(\mathbf{k}) c_{\eta, \mathbf{k}, \mathbf{Q}} \quad (3.37)$$

### 3.2.3 Obtaining Parameters from ab-initio Calculation

For brevity, we just quickly go through a methodology introduced in literature<sup>[34][33]</sup>, which belongs to the family of linear least-square methods. From DFT calculation, we obtain the numerical matrix of Hamiltonian denoted by  $h_{ij}^{\text{DFT}}(\mathbf{k})$ , which is evaluated at a subset of momenta in 1BZ (denoted by  $\mathcal{M}$ ). Our purpose is to find a Hamiltonian that can be expressed in an explicit form like Eq. (3.27) and matches the results of first principle study. Our continuum model can be written in an abstract form:

$$h_{ij}(\mathbf{k}) = \sum_{\alpha=1}^d \lambda_{\alpha} h_{\alpha;ij}(\mathbf{k}) \quad (3.38)$$

where  $h_{\alpha;j}(\mathbf{k})$  is the symmetry constrained basis and  $d$  is the dimension of the basis. We choose a very simple cost function:

$$C_0(\{\lambda_\alpha\}) = \sum_{\mathbf{k} \in \mathcal{M}} \text{Tr} \left[ (h(\mathbf{k}) - h^{\text{DFT}}(\mathbf{k}))^2 \right] \quad (3.39)$$

The rest of our task is to minimize the cost function, which can be expressed in a quadratic form:

$$C_0(\{\lambda_\alpha\}) = \sum_{\alpha, \beta=1}^d A_{\alpha\beta}^{(0)} \lambda_\alpha \lambda_\beta - 2 \sum_{\alpha=1}^d B_\alpha^{(0)} \lambda_\alpha + C^{(0)} \quad (3.40)$$

In Eq. (3.40), we define

$$A_{\alpha\beta}^{(0)} = \text{Re} \left[ \sum_{\mathbf{k} \in \mathcal{M}} \text{Tr} (h_\alpha(\mathbf{k}) h_\beta(\mathbf{k})) \right], \quad (3.41)$$

$$B_\alpha^{(0)} = \sum_{\mathbf{k} \in \mathcal{M}} \text{Tr} (h_\alpha(\mathbf{k}) h^{\text{DFT}}(\mathbf{k})), \quad (3.42)$$

$$C^{(0)} = \sum_{\mathbf{k} \in \mathcal{M}} \text{Tr} (h^{\text{DFT}}(\mathbf{k}) h^{\text{DFT}}(\mathbf{k})). \quad (3.43)$$

It is straight to show that cost function reaches the minimum for value

$$\lambda_\alpha = \left[ \left( A^{(0)} \right)^{-1} B^{(0)} \right]_\alpha \quad (3.44)$$

In this way, one can obtain the continuum model from DFT data without band structures fitting. We name the model generated by this method as "DFT model".

## 第四章 Superconductivity in 3.65° tWSe<sub>2</sub>

In this chapter, we aim to explore the remarkable emergence of superconductivity in twisted bilayer tungsten diselenide (tWSe<sub>2</sub>) at 3.65°. Here we first summarize the key experimental observations<sup>[20][40]</sup> that establish the unconventional characters of the superconducting phase, then outline our theoretical framework—based on a continuum electronic model derived from density-functional theory (DFT) and augmented by a screened Coulomb interaction, through which we compute the Hartree Fock phase diagrams of the normal states at finite temperature, aiming to capture the insulator–metal quantum phase transition driven by the increasing displacement field, and finally benchmark our results against the existing reference second harmonic model. Both our DFT model and second harmonic model have been discussed in chapter 三. We have also noticed that there are recent theoretical studies regarding this topic, based on the three orbital effective tight binding model<sup>[41]</sup> or the second harmonic model with screened Coulomb potential<sup>[42]</sup>. We will not dive into the existing theories of superconductivity in 3.65° tWSe<sub>2</sub> in our article.

### 4.1 Experimental Motivation and Unconventional Signals

In this section, we will show the experimental results based on a recent experiment<sup>[41]</sup>. Unlike conventional superconductors where phonon-mediated pairing dominates, the superconducting states in tWSe<sub>2</sub> emerge near half-filling of the moiré valence band near zero displacement field, distinctly separated from the van Hove singularity (vHS), suggesting a pairing mechanism fundamentally rooted in electronic correlations and other unconventional pairing mechanisms rather than conventional electron-phonon coupling. This is further supported by the system’s behavior in the normal state, which exhibits characteristics of a strongly correlated metal with dramatically renormalized electronic properties, indicative of proximity to a quantum critical point. The superconducting transition itself follows BKT phase transitions of two dimensional systems, with signatures of vortex-dominated phase fluctuations. More evidence of BKT phase transition is shown in Fig.3 of Ref<sup>[41]</sup>. People have observed two critical magnetic fields  $B_{c1}$  and  $B_{c2}$  in the experiment, denoting the magnetic fields which break the zero resistance state and the Cooper pairing, respectively. Note that the signal of Cooper pairs breaking is that the resistance reaches 80% of the resistance of the normal states. And experimentalists find that the resistance of the system between two critical magnetic fields is

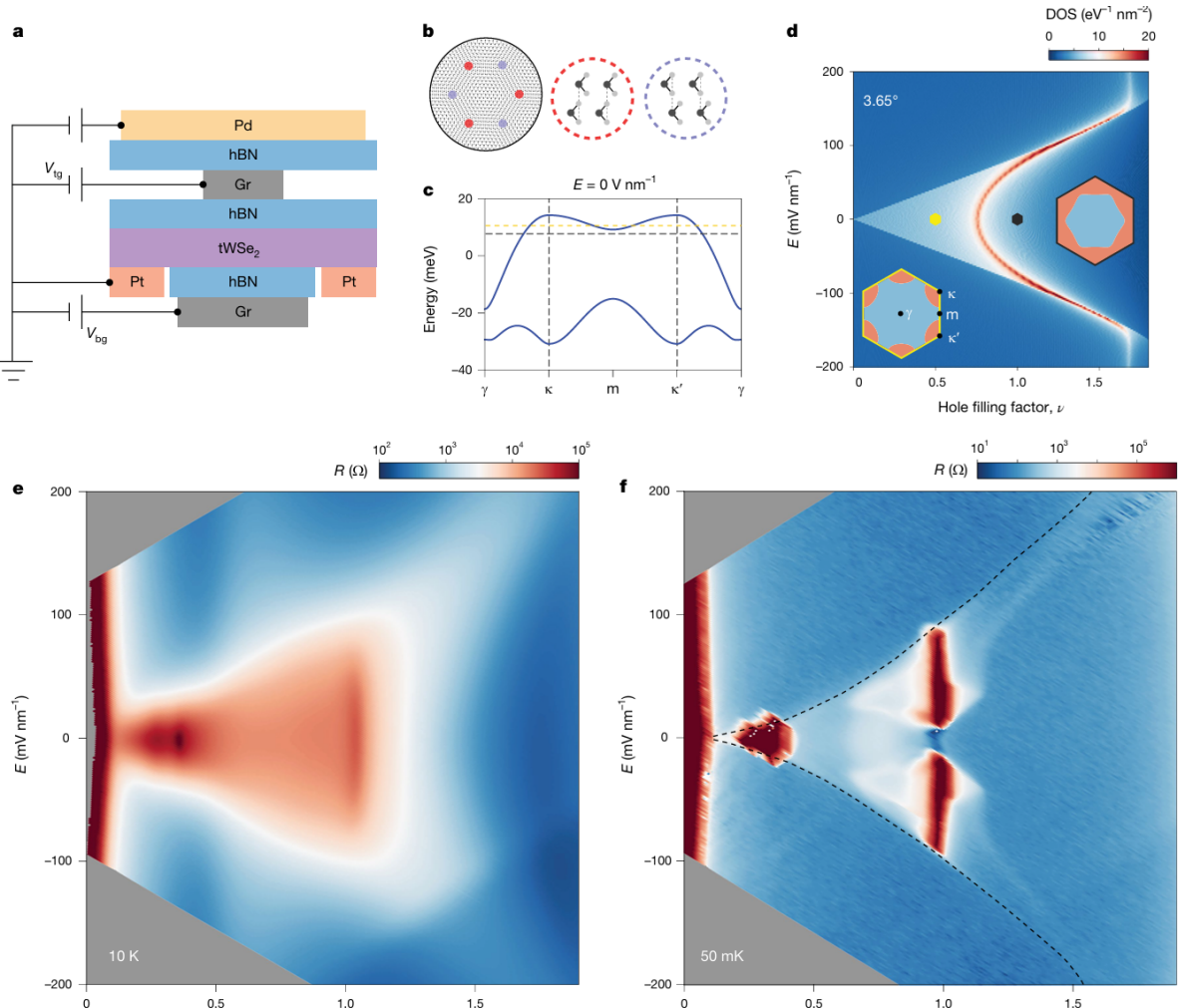


图 4.1 The Fig.1 in literature<sup>[41]</sup>. (a) Schematic of a dual-gated tWSe<sub>2</sub> device. Both gates are made of hexagonal boron nitride (hBN) and few-layer graphite (Gr) with the narrower top gate defining the tWSe<sub>2</sub> channel. The top-gate and bottom-gate voltages ( $V_{tg}$  and  $V_{bg}$ , respectively) control the vertical electric field  $E$  and hole filling factor  $\nu$  in tWSe<sub>2</sub>. (b) Hexagonal moiré lattice of tWSe<sub>2</sub> with MX (red) and XM (blue) stacking sites. The black and grey dots denote the M (W) and X (Se) atoms, respectively. (c) Topmost valence bands for the  $K$  valley state of  $3.65^\circ$  from the second harmonic model Eq. (3.34). Both bands carry Chern number +1. The corresponding bands of the  $K$  valley state carry Chern number -1. The dashed lines mark the Fermi levels corresponding to the dots of the same colour in d. (d) Electronic density of states (DOS) versus electrical field and the hold filling factor. The vHS ( $\approx 0.75$  at  $E=0$ ) disperses towards higher  $\nu$  with increasing  $E$ . Insets: the Fermi surface at  $E=0$  evolves from disconnected hole pockets centred at  $/$  of the moiré Brillouin zone (yellow) to a single electron pocket centred at  $\gamma$  (black) as  $\nu$  passes the vHS. (e)(f) Longitudinal resistance  $R$  as a function of  $E$  and  $\nu$  at  $10K$  (e) and  $50mK$  (f) The dashed lines in f (a guide to the eye) separate the layer-hybridized and layer-polarized regions.

characterized by  $R \propto \frac{B}{B_{c2}}$ , aligning well with the theoretical prediction of the behavior of free vortices, which is discussed in chapter 2: the resistance contributed by the free vortices is proportional to the number of vortices. The number of free vortices is characterized by  $\frac{B}{\Phi_0}$  where  $\Phi_0$  is the magnetic flux quantum, indicating the vortices' contribution is proportional to  $B$ .

The significance of the unconventional superconductivity in  $3.65^\circ$  tWSe<sub>2</sub> extends beyond tWSe<sub>2</sub> itself, offering new insights into the general mechanisms of strongly correlated superconductivity. The material provides a unique testbed to explore open questions about the role of quantum criticality, the nature of pairing in systems with strong spin-orbit coupling, and the emergence of superconductivity from correlated insulating states. Unlike twisted bilayer graphene where superconductivity appears under different doping conditions, the superconductivity of tWSe<sub>2</sub> system possesses a strong doping dependence, demonstrating how specific combinations of spin-orbit interactions, electronic correlations, and moiré band topology can stabilize unconventional superconducting states. Additionally, the intervalley coherence order in the strongly correlated insulating states, reminds us about the importance of intervalley coupling. These observations have broad implications for our understanding of quantum materials, suggesting new pathways to engineer superconducting states through band structure design and highlighting the rich physics that emerges when strong correlation, spin-orbit coupling in moiré transition metal dichalcogenides.

## 4.2 Self consistent HF results for $\theta = 3.65^\circ$ tWSe<sub>2</sub>

In this section, we first construct a DFT model of  $3.65^\circ$  tWSe<sub>2</sub> with double gated screened Coulomb potential. We write down a hole-type Hamiltonian in plane wave basis, then projecting this Hamiltonian into the subspace spanned by three topmost valence bands from  $K$  and  $K'$  valley respectively. In the next two subsections, we present a inspiring formalism to apply mean field approximation and derive the expression of the Hartree Fock potential in our projected Hamiltonian. After that, we list our numerical results of Hartree Fock calculation on the normal states at finite temperature and compare the phase diagrams obtained from the DFT model and the second harmonic model. In this way, we are able to verify the validity of our DFT model, providing us with a ideal platform to perform further calculation to detect the mechanism behind the unconventional superconductivity.

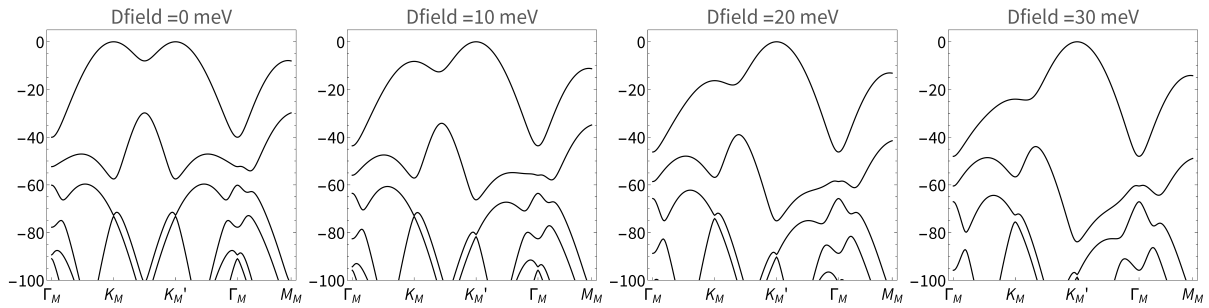


图 4.2 Band structures of  $K$  valley single particle Hamiltonian with different displacement fields  $D\text{field}=0, 10, 20, 30 \text{ meV}$ . The energy is in a scale of meV while the top of valence bands is set to be zero. The twist angle  $\theta$  is fixed to be  $3.65^\circ$  in the rest of the article. The electron bands generated from our continuum model fit the band structures obtained through first principal calculation well.

#### 4.2.1 Interaction in continuum model

The  $K$  valley single-particle Hamiltonian used in our Hartree-Fock calculations is a continuum model extracted from the DFT data of twisted bilayer WSe<sub>2</sub>. We name this continuum model as "DFT model". We perform DFT calculations at two commensurate angles  $\theta = 3.87898^\circ, 3.47156^\circ$ , from which we extract the parameters of the model. We then use the average of the parameter values at two angles to build the continuous model at  $\theta = 3.65^\circ$ . The single particle Hamiltonian is denoted by  $h_{\mathbf{Q},\mathbf{Q}'}^\eta$  to maintain the consistency of notation defined in Section 3.2.1. Since the Hamiltonian from  $K'$  valley is the time reversal counterpart of Hamiltonian from  $K$  valley, we have

$$h_{\mathbf{Q},\mathbf{Q}'}^{-\eta}(\mathbf{k}) = h_{-\mathbf{Q},-\mathbf{Q}'}^{\eta*}(-\mathbf{k}) \quad (4.1)$$

It's also very convenient to include the displacement field  $D$  by adding terms  $\eta \frac{D}{2}(-)^{\mathbf{Q}} \delta_{\mathbf{Q},\mathbf{Q}'}$  to the  $\eta$  valley. Fig. 4.2 shows the band structures generated by the DFT model with varying displacement fields  $D$ .

However, though the band structures almost fit the ab-initio band structures nearly perfectly well, the single particle model is not able to catch some of the most important features of the experimental results in Fig. 4.1. In order to uncover the emergent phenomena arising from strong electronic correlation, we need to add interaction potential to our DFT model. We aim to perform Hartree Fock calculations on normal states at finite temperature based on the many body Hamiltonian with interaction, expecting to reproduce the phenomena observed in the experiment<sup>[41]</sup>.

Double gate screened Coulomb potential is an appropriate candidate of interaction potential. And we are determined to take the screened Coulomb potential with a gate distance

$\xi = 10nm$  in our HF calculation to align with the experimental setup. The double-gated screened Coulomb potential with gate distance  $\xi$  is

$$V(\mathbf{q}) = \pi\xi^2 U_\xi \frac{\tanh(\xi|\mathbf{q}|/2)}{\xi|\mathbf{q}|/2}, \quad V(\mathbf{r}) = U_\xi \sum_{n=-\infty}^{\infty} \frac{(-1)^n}{\sqrt{(\mathbf{r}/\xi)^2 + n^2}} \quad (4.2)$$

where  $U_\xi = e^2/(4\pi\epsilon\xi)$ . The expression for the double-gated screened Coulomb potential can be derived from the potential field generated by an electron placed between two infinitely large metallic plates separated by a distance of  $\xi$ . Specifically, the calculation can be performed using the electrical images method.

In this way, our second quantized continuum model with interaction can be expressed as

$$H_e = \sum_{\mathbf{k}, \mathbf{Q}, \mathbf{Q}'} h_{\mathbf{Q}, \mathbf{Q}'}^\eta(\mathbf{k}) c_{\eta, \mathbf{k}, \mathbf{Q}}^\dagger c_{\eta, \mathbf{k}, \mathbf{Q}'} + \frac{1}{2\Omega_{tot}} \sum_{\mathbf{q}, \mathbf{k}, \mathbf{k}'} \sum_{\eta, \eta'} \sum_{\mathbf{Q}, \mathbf{Q}'} V(\mathbf{q}) c_{\eta, \mathbf{k}+\mathbf{q}, \mathbf{Q}}^\dagger c_{\eta', \mathbf{k}'-\mathbf{q}, \mathbf{Q}'}^\dagger c_{\eta', \mathbf{k}', \mathbf{Q}'} c_{\eta, \mathbf{k}, \mathbf{Q}} \quad (4.3)$$

The second term in Eq. (4.3) is the interaction potential  $V_{int}$ . Our analysis mainly focuses on the physics of topmost valence bands at hole filling factor 1 (i.e.,  $\nu = -1$ ) in this section, the hole Hamiltonian is a more suitable choice for us. The expression of the hole Hamiltonian is slightly different from the electron Hamiltonian:

$$H_h = \sum_{\mathbf{k}, \mathbf{Q}, \mathbf{Q}'} (-h_{\mathbf{Q}, \mathbf{Q}'}^\eta(\mathbf{k})) \tilde{c}_{\eta, \mathbf{k}, \mathbf{Q}}^\dagger \tilde{c}_{\eta, \mathbf{k}, \mathbf{Q}'} + \frac{1}{2\Omega_{tot}} \sum_{\mathbf{q}, \mathbf{k}, \mathbf{k}'} \sum_{\eta, \eta'} \sum_{\mathbf{Q}, \mathbf{Q}'} V(\mathbf{q}) \tilde{c}_{\eta, \mathbf{k}+\mathbf{q}, \mathbf{Q}}^\dagger \tilde{c}_{\eta', \mathbf{k}'-\mathbf{q}, \mathbf{Q}'}^\dagger \tilde{c}_{\eta', \mathbf{k}', \mathbf{Q}'} \tilde{c}_{\eta, \mathbf{k}, \mathbf{Q}} \quad (4.4)$$

where  $\tilde{c}_{\eta, \mathbf{k}, \mathbf{Q}}^\dagger$  denotes the creation operator of holes. The hole creation operator can be related to the electron annihilation operator by a complex conjugate transformation, and these two types of Hamiltonian are actually equivalent up to now. They may differ by a constant energy shift, which dose not affect the final outcome<sup>[36][37]</sup>.

To facilitate numerical computation, the hole Hamiltonian must be projected onto a finite set of bands. The relation between the hole-type creation operator in the projected basis and the original plane-wave basis is given by:

$$\tilde{\gamma}_{\mathbf{k}, n, \eta}^\dagger = \sum_{\mathbf{Q}} U_{\mathbf{Q}, n}^\eta(\mathbf{k}) \tilde{c}_{\eta, \mathbf{k}, \mathbf{Q}}^\dagger \quad (4.5)$$

$U_{\mathbf{Q}, n}^\eta(\mathbf{k})$  is the  $\mathbf{Q}$  component of single particle Hamiltonian's eigenvectors with band index  $n$ . To simplify the expression of Hamiltonian, we can utilize the form factor (also known as overlap matrix)

$$M_{mn}^\eta(\mathbf{k}, \mathbf{q}) = [U_m^\eta(\mathbf{k} + \mathbf{q})]^\dagger U_n^\eta(\mathbf{k}) \quad (4.6)$$

Although our DFT is only well defined in the first moiré Brillouin zone, we can generalize it

to the whole momentum space by applying the embedding condition:

$$U_{\mathbf{Q},m}^{\eta}(\mathbf{k} + \mathbf{G}) = \sum_{\mathbf{Q}'} V_{\mathbf{Q},\mathbf{Q}'}(\mathbf{G}) U_{\mathbf{Q}',m}^{\eta}(\mathbf{k}) \quad (4.7)$$

where  $\mathbf{G}$  is the reciprocal moiré lattice vector and the embedding matrix  $V_{\mathbf{Q},\mathbf{Q}'}$  is defined as

$$V_{\mathbf{Q},\mathbf{Q}'}(\mathbf{G}) = \delta_{\mathbf{Q}',\mathbf{Q}+\mathbf{G}} \quad (4.8)$$

Then the projected interaction potential can be expressed with the form factors:

$$V_{mm'n'n}^{\eta\eta'}(\mathbf{k}, \mathbf{k}', \mathbf{q}) = \frac{1}{\Omega_{tot}} \sum_{\mathbf{G}} V(\mathbf{q} + \mathbf{G}) M_{mn}^{\eta}(\mathbf{k}, \mathbf{q} + \mathbf{G}) M_{n'm'}^{\eta'*}(\mathbf{k}' - \mathbf{q}, \mathbf{q} + \mathbf{G}) \quad (4.9)$$

so that the full hole Hamiltonian now can be written in a projected band basis as:

$$\begin{aligned} H_h = & \sum_{\mathbf{k}, n \leq N_b, \eta} \tilde{\gamma}_{\mathbf{k}, n, \eta}^{\dagger} \tilde{\gamma}_{\mathbf{k}, n, \eta}(-E_n^{\eta}(\mathbf{k})) \\ & + \frac{1}{2} \sum_{\mathbf{k}, \mathbf{k}', \mathbf{q}} \sum_{\eta \eta'} \sum_{mm'n'n \leq N_b} V_{mm'n'n}^{\eta\eta'}(\mathbf{k}, \mathbf{k}', \mathbf{q}) \tilde{\gamma}_{\mathbf{k}+\mathbf{q}, m, \eta}^{\dagger} \tilde{\gamma}_{\mathbf{k}'-\mathbf{q}, m', \eta'}^{\dagger} \tilde{\gamma}_{\mathbf{k}', n', \eta'} \tilde{\gamma}_{\mathbf{k}, n, \eta} \end{aligned} \quad (4.10)$$

where  $N_b$  in Eq. (4.10) represents the number of projected bands. It should be noted that the hole and electron Hamiltonians are no longer equivalent when the basis is reduced to a finite number of bands. Considering this, we will perform Hartree Fock calculations only based on the Hole Hamiltonian.

#### 4.2.2 Mean Field Approximation

In this subsection, we will derive the mean field Hamiltonian  $H_{MF}$  through the variational method. At zero temperature  $T = 0$ , our task is to find a suitable wavefunction of the ground state, whose expectation value of energy is the lowest among all the trial wavefunctions. At finite temperature, a better choice for us is to find the density matrix  $\rho(\lambda)$  with the lowest free energy  $F = E - TS$ , where  $\lambda$  is a tunable parameter.

It is reasonable to assume that the equilibrium density matrix  $\rho_{MF}(\lambda)$  of an auxiliary mean field Hamiltonian  $H_{MF} = H_0 + V_{MF}$  is a good approximation of the equilibrium density matrix of the Hamiltonian with interaction potential  $H = H_0 + V_{int}$ , where  $H_0$  and  $V_{MF}$  are at single-particle level while  $V_{int}$  is a two-body interaction term. Suppose that  $V_{MF}$  is given by the form ( $X$  is a single particle operator>):

$$V_{MF} = \lambda X \quad (4.11)$$

We can generalize this expression later, replacing  $\lambda X$  by  $V_{MF} = \sum_i \lambda_i X_i$ , but now we only

focus on the simplified version of the mean field potential. Note that

$$\rho_{MF}(\lambda) = \frac{e^{-\beta H_{MF}}}{\text{Tr}(e^{-\beta H_{MF}})} \quad (4.12)$$

$$F_{MF} = -k_B T \ln \text{Tr}(e^{-\beta H_{MF}}) \quad (4.13)$$

Using  $V_{MF} = \lambda X$ , we'll reach the conclusion that

$$\frac{\partial F_{MF}}{\partial \lambda} = \text{Tr}(\rho_{MF}(\lambda)X) = \langle X \rangle_{MF} \quad (4.14)$$

For our target  $\lambda$ , we have  $\frac{\partial F[\rho_{MF}(\lambda)]}{\partial \lambda} = 0$ , which means

$$\frac{\partial}{\partial \lambda}(F[\rho_{MF}(\lambda)] - F_{MF}) = \frac{\partial}{\partial \lambda}(\langle V_{int} - V_{MF} \rangle_{MF}) = -\langle X \rangle_{MF} \quad (4.15)$$

Then we obtain a very useful result:

$$\frac{\partial}{\partial \lambda}\langle V_{int} \rangle_{MF} = \lambda \frac{\partial}{\partial \lambda}\langle X \rangle_{MF} \quad (4.16)$$

Replacing  $V_{MF}$  by  $\sum_i \lambda_i X_i$ , it is easy to derive that

$$\lambda_i = \frac{\partial \langle V_{int} \rangle_{MF}}{\partial \langle X_i \rangle_{MF}} \quad (4.17)$$

This equation provides us with a effective way to apply mean field approximation. If the  $X_i$  refers to the  $\langle c^\dagger c \rangle$  like terms, we will obtain the Hartree Fock potential while the  $X_i$  refers to the  $\langle c^\dagger c^\dagger \rangle$  or  $\langle cc \rangle$  like terms, we will get the mean field approximation of superconducting Hamiltonian, which is shown in Section 2.1.2.

#### 4.2.3 Hartree Fock Potential

Assuming there is no translational symmetry breaking in our calculation of tWSe<sub>2</sub>, the order parameter in momentum space then can be defined as  $\langle \tilde{\gamma}_{\mathbf{k}',m,\eta}^\dagger \tilde{\gamma}_{\mathbf{k}',n',\eta'} \rangle$ , which can be thought as the  $X_i$  in Eq. (4.17):

$$\begin{aligned} \Sigma_H &= \frac{1}{2} \sum_{\mathbf{k}, \mathbf{k}'} \sum_{\eta, \eta'} \sum_{mm'n'n} V_{mm'n'n}^{\eta\eta'}(\mathbf{k}, \mathbf{k}', \mathbf{q} = 0) \\ &\times (\langle \tilde{\gamma}_{\mathbf{k},m,\eta}^\dagger \tilde{\gamma}_{\mathbf{k},n,\eta} \rangle \tilde{\gamma}_{\mathbf{k}',m',\eta',n',\eta'}^\dagger + \tilde{\gamma}_{\mathbf{k},m,\eta}^\dagger \tilde{\gamma}_{\mathbf{k},n,\eta} \langle \tilde{\gamma}_{\mathbf{k}',m',\eta',n',\eta'}^\dagger \rangle) \end{aligned} \quad (4.18)$$

$$\begin{aligned} \Sigma_F &= -\frac{1}{2} \sum_{\mathbf{k}, \mathbf{k}'} \sum_{\eta, \eta'} \sum_{mm'n'n} V_{mm'n'n}^{\eta\eta'}(\mathbf{k}, \mathbf{k}', \mathbf{k}' - \mathbf{k}) \\ &\times (\langle \tilde{\gamma}_{\mathbf{k}',m,\eta}^\dagger \tilde{\gamma}_{\mathbf{k}',n',\eta'} \rangle \tilde{\gamma}_{\mathbf{k},m',\eta',n',\eta'}^\dagger + \tilde{\gamma}_{\mathbf{k}',m,\eta}^\dagger \tilde{\gamma}_{\mathbf{k}',n',\eta'} \langle \tilde{\gamma}_{\mathbf{k},m',\eta',n',\eta'}^\dagger \rangle) \end{aligned} \quad (4.19)$$

In this way, the mean field interacting Hamiltonian takes the form of  $H_{MF} = H_0 + \Sigma_H + \Sigma_F$ . We are able to further simplify the expression above using the fermionic nature of the holes:

$$V_{mm'n'n}^{\eta\eta'}(\mathbf{k}, \mathbf{k}', \mathbf{q}) = V_{m'mn'n}^{\eta'\eta}(\mathbf{k}', \mathbf{k}, -\mathbf{q}) \quad (4.20)$$

This property results in the simplification of the Hartree Fock potential

$$(\Sigma_H)_{mn}^{\eta\eta''}(\mathbf{k}) = \sum_{\mathbf{k}'} \sum_{\eta'} \sum_{m'n'} V_{mm'n'n}^{\eta\eta'}(\mathbf{k}, \mathbf{k}', 0) \langle \tilde{\gamma}_{\mathbf{k}', m', \eta'}^\dagger \tilde{\gamma}_{\mathbf{k}' n', \eta'} \rangle \delta_{\eta, \eta''} \quad (4.21)$$

$$(\Sigma_F)_{m'n}^{\eta'\eta}(\mathbf{k}) = - \sum_{\mathbf{k}'} \sum_{mn'} V_{mm'n'n}^{\eta\eta'}(\mathbf{k}, \mathbf{k}', \mathbf{k}' - \mathbf{k}) \langle \tilde{\gamma}_{\mathbf{k}', m, \eta}^\dagger \tilde{\gamma}_{\mathbf{k}' n', \eta'} \rangle \quad (4.22)$$

It is evident that the mean field Hamiltonian can be described by the values of order parameters  $\langle \tilde{\gamma}_{\mathbf{k}, m, \eta}^\dagger \tilde{\gamma}_{\mathbf{k}, n, \eta'} \rangle$ . Under many circumstances, we need to perform our computation on a relatively small lattice (such as  $6 \times 6, 12 \times 12$ ), thus the order parameters obtained through self-consistent calculation is only accessible on a sparse lattice of 1BZ. But in Eq. (4.21) and Eq. (4.22) we find, once we obtain the value of order parameters labeled by  $\mathbf{k}'$ , we are able to evaluate the non-self-consistent Hamiltonian on a dense mesh of wavevectors labeled by  $\mathbf{k}$ , which is irrelevant to the original lattice. Therefore, it is possible to get a "smooth" band structure based on a small lattice<sup>[43][44][45]</sup>. The comparison can be seen in Fig. 4.3.

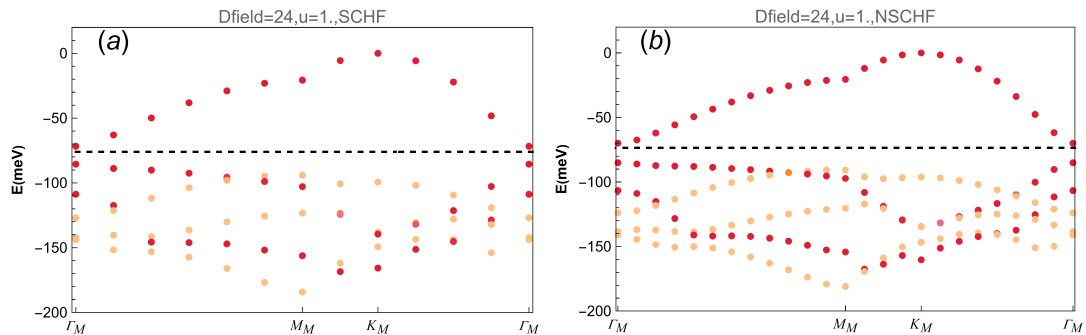


图 4.3 Band structures generated by the self-consistent Hamiltonian and the non self-consistent Hamiltonian respectively.(a) The band structure is generated by the self-consistent Hamiltonian of  $u = 10/\epsilon = 1$  and displacement field  $Dfield=24$ . The size of momentum mesh is  $12 \times 12$ , i.e.  $N_1 = 12, N_2 = 12$ .(b) The band structure is generated by the non self-consistent Hamiltonian on a  $24 \times 24$  mesh using the same order parameters in (a). The dashed line represents the Fermi level, and the color of each points in (a)(b) represents the valley polarization of each states which also shows the spin polarization due the the strong spin-orbital coupling. Pure orange represents the K valley polarized states while the pure red is the color of  $K'$  valley.

#### 4.2.4 Numerical results of $\nu = -1$ tWSe<sub>2</sub> Based on DFT Model

With the derived mean field Hamiltonian  $H_{MF}$ , we can perform self consistent Hartree Fock calculation at filling  $\nu = -1$ , i.e. one hole per moiré unit cell. Specifically, we pick three bands from  $K$  and  $K'$  valley respectively (3 bands per valley) to constitute the projected band basis while the gate distance  $\xi$  in the screened Coulomb potential is chosen to be 10. The reference value of dielectric constant  $\epsilon$  is 10 in our phase diagrams so that the strength of interaction is reflected by  $\frac{10}{\epsilon}$ .

In order to perform numerical calculation, the moiré Brillouin is discretized into a 12\*12  $\mathbf{k}$  mesh, where

$$\mathbf{k} = \frac{m}{N_1} \mathbf{b}_{M,1} + \frac{n}{N_2} \mathbf{b}_{M,2} \quad (N_1 = N_2 = 12) \quad (4.23)$$

and m,n are all integers less than 12. To avoid reaching the local minimum, we employed several different initial conditions , such as starting with random real order parameters. Additionally, the iteration algorithm in our calculation is the well known optimal damping algorithm(ODA)<sup>[46]</sup>. Compared with other algorithms such as the Roothaan algorithm<sup>[47]</sup> and level-shifting algorithm<sup>[48]</sup>, the convergence properties of ODA are satisfactory and the computational cost of each iteration is nearly the same as Roothaan algorithm, which is the simplest algorithm. The energy is evaluated by:

$$E_{MF} = \left\langle H_0 + \frac{1}{2} (\Sigma_H + \Sigma_F) \right\rangle_{MF} \quad (4.24)$$

Additionally, in order to shed light on the symmetries of tWSe<sub>2</sub>, we include different types of translational symmetry breaking in our calculation. Unit cell enlargement, or band folding method is widely used in self-consistent calculation<sup>[44][49]</sup>, adding intermomentum coupling in the moiré Brillouin Zone. Now the expectation values of  $\langle \tilde{\gamma}_{\mathbf{k},m,\eta}^\dagger \tilde{\gamma}_{\mathbf{k}+\mathbf{Q},n,\eta} \rangle$  are no longer zero, and we can use a pair of nesting vectors  $\mathbf{Q}_1, \mathbf{Q}_2$  to characterize such symmetry breaking states, giving us the new periods of charge density modulation . Thus we have:

$$\langle \tilde{\gamma}_{\mathbf{k},m,\eta}^\dagger \tilde{\gamma}_{\mathbf{k}+\mathbf{Q},n,\eta} \rangle \neq 0 \quad (\mathbf{Q} = n_1 \mathbf{Q}_1 + n_2 \mathbf{Q}_2, n_1, n_2 \in \mathbb{Z}) \quad (4.25)$$

As a result, the unit cells become  $|\mathbf{b}_{M,1} \times \mathbf{b}_{M,2}| / |\mathbf{Q}_1 \times \mathbf{Q}_2|$  times larger, correspondingly we obtain a folded moiré Brillouin Zone. Such ground states tend to be incompressible, which is shown in the phase diagram of direct gap or indirect gap in Fig. 4.4. In addition, the charge density wave components can be measured by the average Frobenius norm of the order parameter submatrix whose elements take the form  $\langle \tilde{\gamma}_{\mathbf{k}+\mathbf{Q},\eta}^\dagger \tilde{\gamma}_{\mathbf{k}+\mathbf{Q}',\eta} \rangle$ , where  $\mathbf{Q} \neq \mathbf{Q}'$  and  $\mathbf{k}$  is momen-

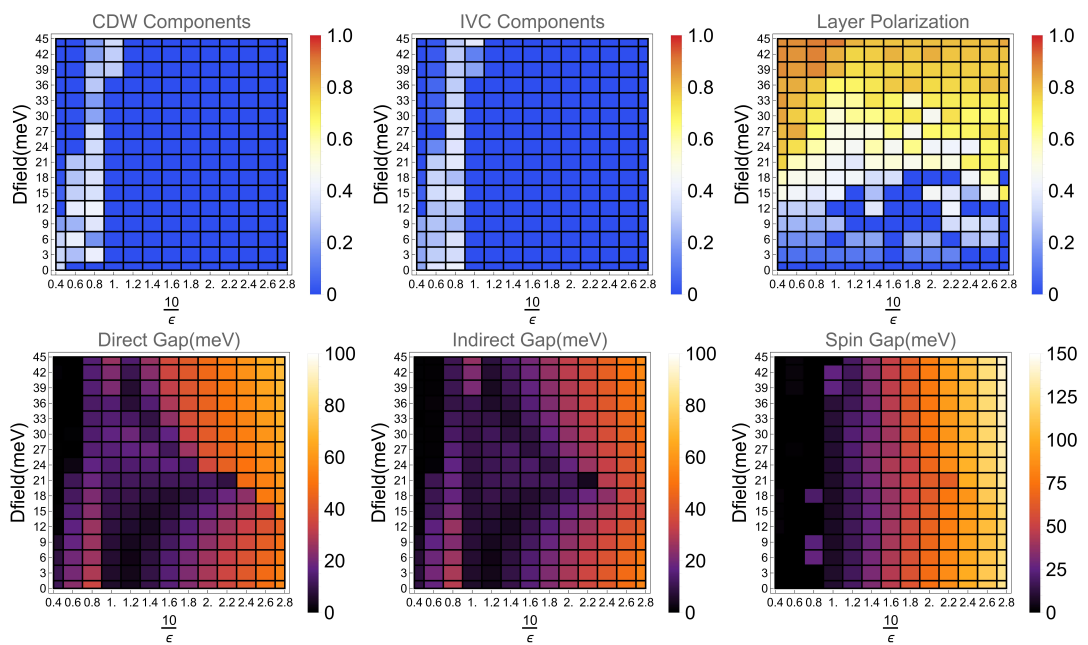


图 4.4 The phase diagrams with varying displacement fields and dielectric constants. CDW components measure the strength of intermomentum coupling, showing possible charge density wave(CDW)-ordered ground states. The phase diagram of IVC components reflects the emergence of IVC order, which also leads to moiré translational symmetry breaking like the CDW order. In the diagram of layer polarization, we can see the tendance of layer polarization in ground states with increasing Dfields. As for the phase diagrams of direct gap and indirect gap, we can see the clear signals of correlated insulator-metal phase transition, aligning with experimental results. The spin gap is about the energy cost of flipping spin, relating to the spin polarization shown in Fig. 4.5.

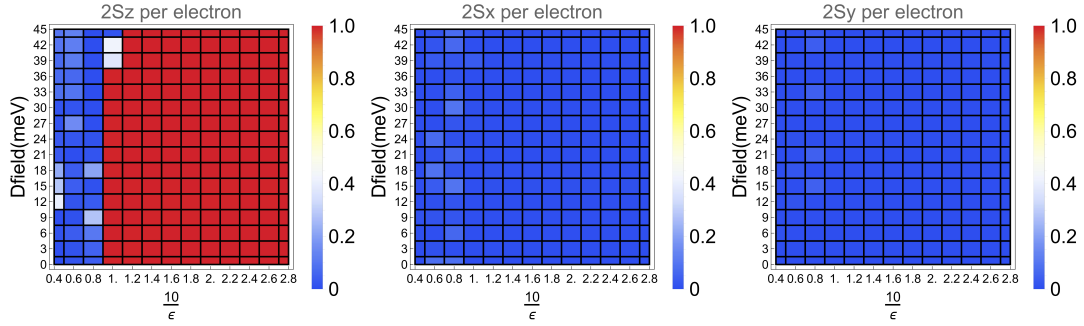


图 4.5 Phase diagrams of spin polarization along each direction. For ground states whose strength of interaction  $\frac{10}{\epsilon}$  is greater than 0.8, they have the inclination of being spin polarized along z direction, while spin along x or y direction is close to zero. Considering the the spin-valley locking nature of tWSe<sub>2</sub>, the phase diagram of z direction spin polarization also reflects the ground states' valley polarization.

tum in the folded moiré Brillouin zone. To be more specific, in our  $n \times n$  type of supercell ,  $\mathbf{Q}_1 = \frac{\mathbf{b}_{M1}}{n}$ ,  $\mathbf{Q}_2 = \frac{\mathbf{b}_{M2}}{n}$ .

To further unravel the mystery of quantum phase transitions of  $3.65^\circ$  tWSe<sub>2</sub>, we take IKS (incommensurate Kekulé spiral) type translational symmetry breaking states into our consideration, diving into another type of lattice distortion<sup>[11][50][51]</sup>. In this type of ground states, there is intervalley coherence with a momentum shift  $\mathbf{q}$ :  $\langle \tilde{\gamma}_{\mathbf{k}+\frac{n\mathbf{q}}{2}, \eta}^\dagger, \tilde{\gamma}_{\mathbf{k}+\frac{n'\mathbf{q}}{2}, \eta'} \rangle$  coming from the valley boost:

$$H_0^\eta(\mathbf{k}) \rightarrow H_0^\eta(\mathbf{k} + \eta \frac{\mathbf{q}}{2}) \quad (4.26)$$

Unlike the normal IVC (intervalley coherence) states leading to a  $\sqrt{3} \times \sqrt{3}$  Kekulé pattern<sup>[52]</sup>, the IKS states with momentum shift  $\mathbf{q}$  preserve modified translational symmetry  $\hat{T}'_{\mathbf{a}_{M,i}}$

$$\hat{T}'_{\mathbf{a}_{M,i}} = \hat{T}_{\mathbf{a}_{M,i}} \exp\left(i\mathbf{q} \cdot \mathbf{a}_{M,i} \frac{\tau_z}{2}\right) \quad (4.27)$$

where  $\hat{T}_{\mathbf{a}_{M,i}}$  is the translation operator of lattice vector  $\mathbf{a}_{M,i}$  and  $\tau_z$  is the Pauli matrix applying to the valley space. In our calculation, we pick up several commensurate wavevectors like  $K_M, M_M$  to perform our numerical computation.

From Fig. 4.5 , we can see the interaction-driven phase transition through the spin phase diagrams. Ferromagnetic phase emerges when dielectric constant  $\epsilon > 10$ . Considering the spin-valley locking nature of tWSe<sub>2</sub>, this can be also seen as a valley polarized region. With a finite spin gap shown in Fig. 4.4, the ferromagnetic states in strong interaction region are robust. On the contrary, in the weak interaction region, intervalley coherence(IVC) order outshines the ferromagnetic order and breaks the  $U(1)$  valley symmetry of  $\pm K$  valley. Due to the spontaneous breaking of  $U(1)$  symmetry , a larger gap is favored for  $\frac{10}{\epsilon} < 1$ . In the exper-

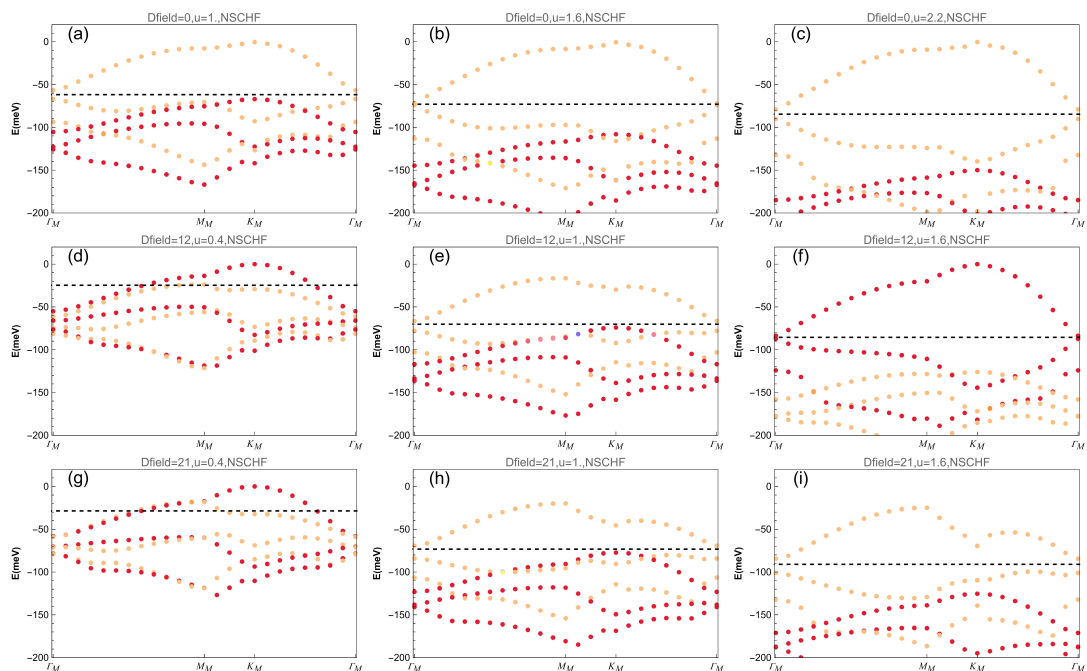


图 4.6 Band structures with different interaction strength and displacement fields Dfield. The meaning of color is the same as the color in Fig. 4.3. In figure (d)(g), we can observe gap closing and band mixing from  $K$  and  $K'$  valley, which suggests the emergence of intervalley coherence. Another thing in common is the small Hartree Fock gap at  $\Gamma_M$  point in every band structures, which is different from the results generated by the second harmonic model shown later in Section 4.2.5.

iment, the correlated insulator-metal phase transition with the increasing displacement field was observed. Additionally, the observed correlated insulating phase had IVC order, and this key feature is captured by our numerical simulation in the weak interaction  $\frac{10}{\epsilon} < 0.8$ .

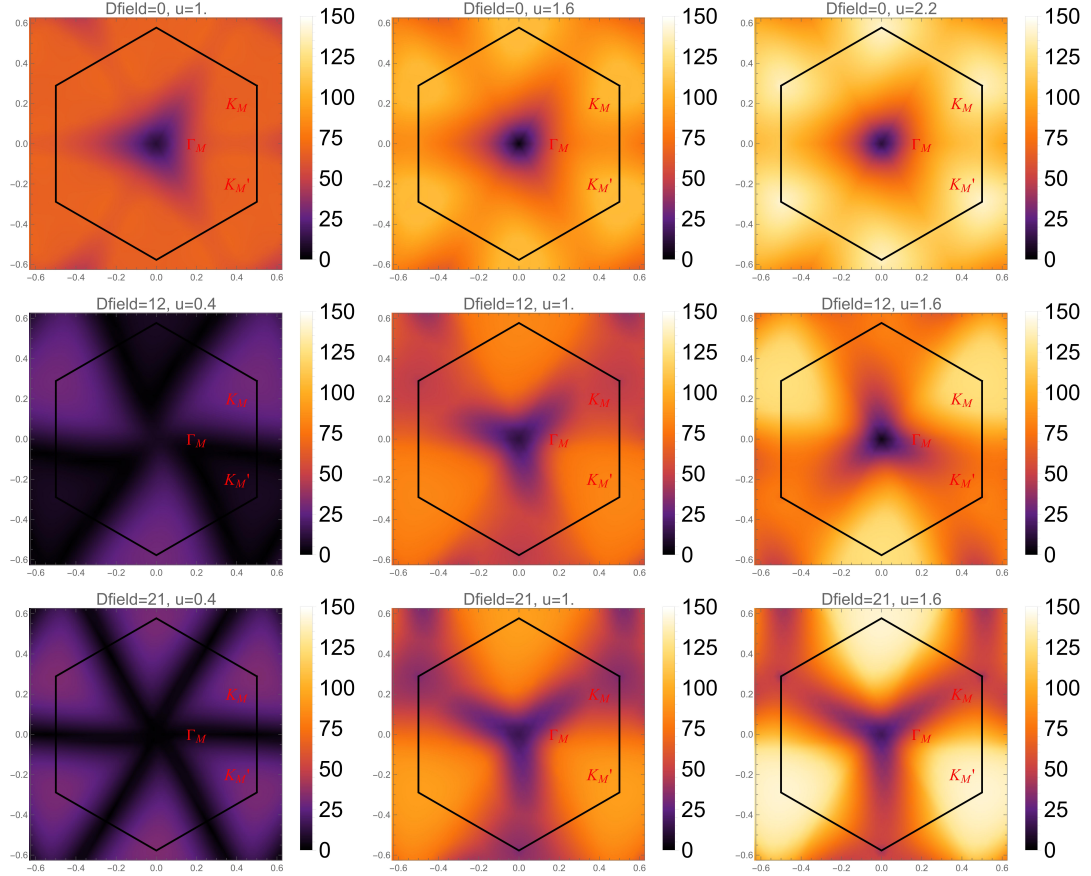


图 4.7 Direct gap over the moiré Brillouin zone of the ground states preserving translational symmetry, with vary displacement fields and interaction strengths  $u$ . We can not witness the signal of spontaneous crystalline symmetry breaking in these states, such as  $C_{3z}$  symmetry breaking.

#### 4.2.5 Benchmark

In this subsection, we will make a comparison between our DFT model and the second harmonic model introduced in chapter 三. Based on Fig. 4.8, we claim that both models are able to catch the features of top two valence bands from  $K$  valley. However, the third valence bands from these two models behave differently and our DFT model fits ab-initio calculation better. If we pick three bands per valley in our Hartree-Fock calculations (which is the case in Section 4.2.4), the behavior of the third valence bands is important. The comparison of Hartree-Fock band structures shown in Section 4.2.5 also suggests that our DFT model is more suitable. Besides, Hartree Fock band structures of our DFT model has a smaller gap.

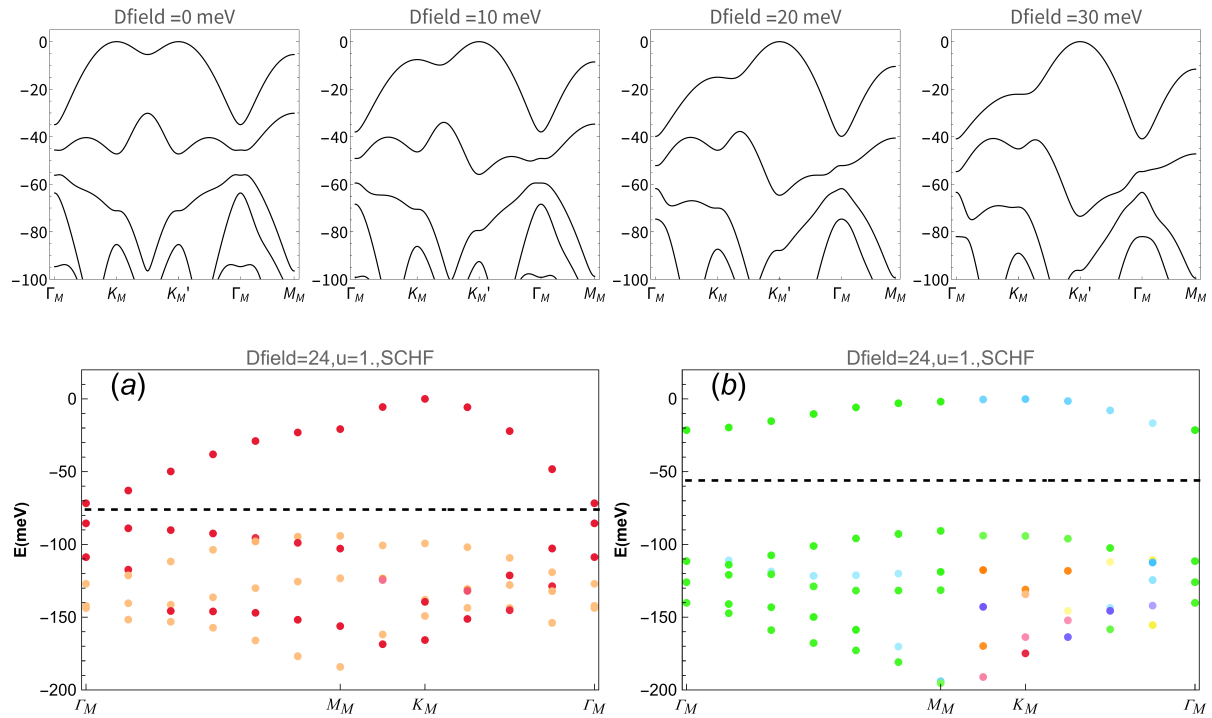


图 4.8 The first row demonstrates the  $K$  valley band structures of second harmonic model of  $3.65^\circ$  tWSe<sub>2</sub>. In the comparison with Fig. 4.2, we find that the second harmonic model fits well with the top two bands well, but falls short in the description of other bands. The second row is the Hartree Fock band structure of DFT model and second harmonic model at Dfield=24mev,  $u=1$ . We pick two bands per valley and perform Hartree Fock calculation on a  $6*6$  k-mesh. Obviously, they are utterly different, either in the valley polarization or in the band gap at  $\Gamma_M$  point.

## 第五章 Conclusion and Outlook

This thesis has systematically investigated the unconventional superconductivity and correlated phases in twisted bilayer WSe<sub>2</sub> at the twist angle 3.65°, integrating theoretical frameworks, ab-intio based modeling, and advanced numerical methods. Beginning with the famous BCS theory and BKT theory of 2D superconductivity, we found the bridges between the theoretical predictions and the experimental observations in tWSe<sub>2</sub>, where sharp resistance drops and vortex-dominated critical behavior align with universal 2D superconducting transitions<sup>[41]</sup>. In chapter 3, through rigorous analysis of AA/AB stacking configurations, we derived interlayer hopping matrices via two complementary approaches: the two-center approximation and symmetry-constrained derivation based on symmetries ( $C_{3z}$ ,  $C_{2y}\mathcal{T}$ , etc.). The development of a symmetry-guided, DFT model in Chapter 3 provided a high-precision tool to capture moiré band topology of low energy physics<sup>[34]</sup>. By incorporating double-gated electrostatic screening, our model connected the atomic-scale details with emergent quantum phenomena, enabling realistic simulations of correlated states.

In Chapter 4, self-consistent Hartree-Fock calculations on the normal states at hole filling  $|v| = 1$  revealed a displacement field driven insulator-metal transition, consistent with experiments. Multiple moiré translational symmetry breaking orders—including charge density waves, intervalley coherence (IVC), and Kekulé spiral (IKS) order—were identified. Strong interaction  $10/\epsilon > 1$  favors spin-valley polarized ferromagnetic phases, while weaker interaction stabilizes IVC-ordered correlated insulators. The DFT model's superiority over the second harmonic approach was evident in its accurate prediction of band structures and phase diagrams, underscoring the importance of first-principles parameterization.

While this work elucidates the normal-state phase diagram, the microscopic pairing mechanism of superconductivity in tWSe<sub>2</sub> remains unresolved. A critical next step involves probing dynamical spin fluctuations in the correlated normal states using time-dependent Hartree-Fock or GW-based methods. These approaches could compute spin susceptibilities to identify whether magnetic interactions drive pairing instabilities, potentially linking the observed superconductivity to spin-fluctuation-mediated mechanisms. Combining GW with dynamical mean-field theory (GW+DMFT) may further unify dynamic screening and strong correlations, enabling direct predictions of gap symmetry and critical temperatures.

Complementary studies using simplified tight binding or heavy fermion models, devel-

oped by collaborators, could bypass the complexity of continuum formalisms. For instance, quantum Monte Carlo simulations on lattice models might reveal competing orders or pairing tendencies inaccessible to mean-field methods. Heavy fermion frameworks, treating flat band electrons as hybridizing with localized moments, could draw parallels to unconventional superconductors like cuprates, where magnetic exchange underpins pairing. The interplay of IVC, CDW, and superconducting fluctuations also warrants exploration. Functional renormalization group (fRG) methods could map competing instabilities across parameter space, while topological invariants of moiré bands—such as Chern numbers—might connect band topology to pairing symmetry. Generalizing this methodology to other TMDs (e.g., MoTe<sub>2</sub>, WS<sub>2</sub>) could uncover universal trends, leveraging variations in spin orbit coupling or stacking configurations to tune between spin fluctuation and phonon-driven superconductivity.

In summary, this thesis establishes a robust foundation for studying correlated phases in moiré TMDs through ab-initio models and many-body techniques. Future work integrating dynamical correlation, model Hamiltonians, and topological insights will advance our understanding of unconventional superconductivity, guiding the design of quantum materials with tailored electronic properties.

## 参考文献

- [1] BARDEEN J, COOPER L N, SCHRIEFFER J R. Theory of Superconductivity[J/OL]. Phys. Rev., 1957, 108: 1175-1204. <https://link.aps.org/doi/10.1103/PhysRev.108.1175>. DOI: 10.1103/PhysRev.108.1175.
- [2] DAGOTTO E. High Temperature Superconductors: A Review[M/OL]//SCHACHINGER E, MITTER H, SORMANN H. Recent Progress in Many-Body Theories: Volume 4. Boston, MA: Springer US, 1995: 319-374. [https://doi.org/10.1007/978-1-4615-1937-9\\_30](https://doi.org/10.1007/978-1-4615-1937-9_30). DOI: 10.1007/978-1-4615-1937-9\_30.
- [3] MCMILLAN W L. Transition Temperature of Strong-Coupled Superconductors[J/OL]. Phys. Rev., 1968, 167: 331-344. <https://link.aps.org/doi/10.1103/PhysRev.167.331>. DOI: 10.1103/PhysRev.167.331.
- [4] ANDREI E Y, MACDONALD A H. Graphene bilayers with a twist[J/OL]. Nature Materials, 2020, 19(12): 1265-1275. <http://dx.doi.org/10.1038/s41563-020-00840-0>. DOI: 10.1038/s41563-020-00840-0.
- [5] BISTRITZER R, MACDONALD A H. Moiré bands in twisted double-layer graphene[J/OL]. Proceedings of the National Academy of Sciences, 2011, 108(30): 12233-12237. eprint: <https://www.pnas.org/doi/pdf/10.1073/pnas.1108174108>. <https://www.pnas.org/doi/abs/10.1073/pnas.1108174108>. DOI: 10.1073/pnas.1108174108.
- [6] WANG Y J, ZHOU G D, PENG S Y, et al. Molecular Pairing in Twisted Bilayer Graphene Superconductivity[J/OL]. Phys. Rev. Lett., 2024, 133: 146001. <https://link.aps.org/doi/10.1103/PhysRevLett.133.146001>. DOI: 10.1103/PhysRevLett.133.146001.
- [7] CHANG C Z, LIU C X, MACDONALD A H. Colloquium: Quantum anomalous Hall effect[J/OL]. Rev. Mod. Phys., 2023, 95: 011002. <https://link.aps.org/doi/10.1103/RevModPhys.95.011002>. DOI: 10.1103/RevModPhys.95.011002.
- [8] SONG Z, WANG Z, SHI W, et al. All Magic Angles in Twisted Bilayer Graphene are Topological [J/OL]. Phys. Rev. Lett., 2019, 123: 036401. <https://link.aps.org/doi/10.1103/PhysRevLett.123.036401>. DOI: 10.1103/PhysRevLett.123.036401.
- [9] PO H C, ZOU L, SENTHIL T, et al. Faithful tight-binding models and fragile topology of magic-angle bilayer graphene[J/OL]. Phys. Rev. B, 2019, 99: 195455. <https://link.aps.org/doi/10.1103/PhysRevB.99.195455>. DOI: 10.1103/PhysRevB.99.195455.
- [10] PO H C, WATANABE H, VISHWANATH A. Fragile Topology and Wannier Obstructions[J/OL]. Phys. Rev. Lett., 2018, 121: 126402. <https://link.aps.org/doi/10.1103/PhysRevLett.121.126402>. DOI: 10.1103/PhysRevLett.121.126402.
- [11] KWAN Y H, WAGNER G, SOEJIMA T, et al. Kekulé Spiral Order at All Nonzero Integer Fillings in Twisted Bilayer Graphene[J/OL]. Phys. Rev. X, 2021, 11: 041063. <https://link.aps.org/doi/10.1103/PhysRevX.11.041063>. DOI: 10.1103/PhysRevX.11.041063.
- [12] EREMETS M I. The current status and future development of high-temperature conventional super-

- conductivity[J/OL]. National Science Review, 2024, 11(7): nwae047. eprint: <https://academic.oup.com/nsr/article-pdf/11/7/nwae047/58227674/nwae047.pdf>. <https://doi.org/10.1093/nsr/nwae047>. DOI: 10.1093/nsr/nwae047.
- [13] MANZELI S, OVCHINNIKOV D, PASQUIER D, et al. 2D transition metal dichalcogenides[J]. Nature Reviews Materials, 2017, 2(8): 1-15.
- [14] ZHU J, CHOU Y Z, XIE M, et al. Superconductivity in twisted transition metal dichalcogenide homobilayers[J/OL]. Phys. Rev. B, 2025, 111: L060501. <https://link.aps.org/doi/10.1103/PhysRevB.111.L060501>. DOI: 10.1103/PhysRevB.111.L060501.
- [15] LIU C X. Unconventional Superconductivity in Bilayer Transition Metal Dichalcogenides[J/OL]. Phys. Rev. Lett., 2017, 118: 087001. <https://link.aps.org/doi/10.1103/PhysRevLett.118.087001>. DOI: 10.1103/PhysRevLett.118.087001.
- [16] ZHANG Y, LIU T, FUL. Electronic structures, charge transfer, and charge order in twisted transition metal dichalcogenide bilayers[J/OL]. Phys. Rev. B, 2021, 103: 155142. <https://link.aps.org/doi/10.1103/PhysRevB.103.155142>. DOI: 10.1103/PhysRevB.103.155142.
- [17] QIAO L Y, JIANG X C, RUAN Z, et al. Tunable magnetism in bilayer transition metal dichalcogenides[J/OL]. Phys. Rev. Mater., 2024, 8: 034003. <https://link.aps.org/doi/10.1103/PhysRevMaterials.8.034003>. DOI: 10.1103/PhysRevMaterials.8.034003.
- [18] REGAN E C, WANG D, PAIK E Y, et al. Emerging exciton physics in transition metal dichalcogenide heterobilayers[J/OL]. Nature Reviews Materials, 2022, 7(10): 778-795. <https://doi.org/10.1038/s41578-022-00440-1>. DOI: 10.1038/s41578-022-00440-1.
- [19] JU L, MACDONALD A H, MAK K F, et al. The fractional quantum anomalous Hall effect[J/OL]. Nature Reviews Materials, 2024, 9(7): 455-459. <https://doi.org/10.1038/s41578-024-00694-x>. DOI: 10.1038/s41578-024-00694-x.
- [20] XIA Y, HAN Z, WATANABE K, et al. Unconventional superconductivity in twisted bilayer WSe<sub>2</sub> [EB/OL]. 2024. <https://arxiv.org/abs/2405.14784>. arXiv: 2405.14784 [cond-mat.mes-hall].
- [21] MORIYA T. Developments of the theory of spin fluctuations and spin fluctuation-induced superconductivity[J]. Proceedings of the Japan Academy, Series B, 2006, 82(1): 1-16. DOI: 10.2183/pjab.82.1.
- [22] BALSEIRO C A, FALICOV L M. Superconductivity and charge-density waves[J/OL]. Phys. Rev. B, 1979, 20: 4457-4464. <https://link.aps.org/doi/10.1103/PhysRevB.20.4457>. DOI: 10.1103/PhysRevB.20.4457.
- [23] STEWART G R. Heavy-fermion systems[J/OL]. Rev. Mod. Phys., 1984, 56: 755-787. <https://link.aps.org/doi/10.1103/RevModPhys.56.755>. DOI: 10.1103/RevModPhys.56.755.
- [24] QI X L, ZHANG S C. Topological insulators and superconductors[J/OL]. Rev. Mod. Phys., 2011, 83: 1057-1110. <https://link.aps.org/doi/10.1103/RevModPhys.83.1057>. DOI: 10.1103/RevModPhys.83.1057.
- [25] SATO M, ANDO Y. Topological superconductors: a review[J/OL]. Reports on Progress in Physics, 2017, 80(7): 076501. <https://dx.doi.org/10.1088/1361-6633/aa6ac7>. DOI: 10.1088/1361-6633/aa6ac7.

- [26] ALTLAND A, SIMONS B D. Condensed Matter Field Theory[M]. 2nd ed. Cambridge University Press, 2010.
- [27] COLEMAN P. Introduction to Many-Body Physics[C/OL]//. 2016. <https://api.semanticscholar.org/CorpusID:123602889>.
- [28] MERMIN N D, WAGNER H. Absence of Ferromagnetism or Antiferromagnetism in One- or Two-Dimensional Isotropic Heisenberg Models[J/OL]. Phys. Rev. Lett., 1966, 17: 1133-1136. <https://link.aps.org/doi/10.1103/PhysRevLett.17.1133>. DOI: 10.1103/PhysRevLett.17.1133.
- [29] HOHENBERG P C. Existence of Long-Range Order in One and Two Dimensions[J/OL]. Phys. Rev., 1967, 158: 383-386. <https://link.aps.org/doi/10.1103/PhysRev.158.383>. DOI: 10.1103/PhysRev.158.383.
- [30] OHTA T, JASNOW D. XY model and the superfluid density in two dimensions[J/OL]. Phys. Rev. B, 1979, 20: 139-146. <https://link.aps.org/doi/10.1103/PhysRevB.20.139>. DOI: 10.1103/PhysRevB.20.139.
- [31] KOSTERLITZ J M. The critical properties of the two-dimensional xy model[J]. J. Phys. C, 1974, 7(6): 1046. DOI: 10.1088/0022-3719/7/6/005.
- [32] VENDITTI G, BISCARAS J, HURAND S, et al. Nonlinear  $I-V$  characteristics of two-dimensional superconductors: Berezinskii-Kosterlitz-Thouless physics versus inhomogeneity[J/OL]. Phys. Rev. B, 2019, 100: 064506. <https://link.aps.org/doi/10.1103/PhysRevB.100.064506>. DOI: 10.1103/PhysRevB.100.064506.
- [33] CĂLUGĂRU D, JIANG Y, HU H, et al. A New Moiré Platform Based on M-Point Twisting[EB/OL]. 2024. <https://arxiv.org/abs/2411.18684>. arXiv: 2411.18684 [cond-mat.str-el].
- [34] ZHANG Y, PI H, LIU J, et al. Universal Moiré-Model-Building Method without Fitting: Application to Twisted MoTe<sub>2</sub> and WSe<sub>2</sub>[EB/OL]. 2024. <https://arxiv.org/abs/2411.08108>. arXiv: 2411.08108 [cond-mat.mes-hall].
- [35] SCHEER M G, GU K, LIAN B. Magic angles in twisted bilayer graphene near commensuration: Towards a hypermagic regime[J/OL]. Phys. Rev. B, 2022, 106: 115418. <https://link.aps.org/doi/10.1103/PhysRevB.106.115418>. DOI: 10.1103/PhysRevB.106.115418.
- [36] YU J, HERZOG-ARBEITMAN J, WANG M, et al. Fractional Chern insulators versus nonmagnetic states in twisted bilayer MoTe<sub>2</sub>[J/OL]. Phys. Rev. B, 2024, 109: 045147. <https://link.aps.org/doi/10.1103/PhysRevB.109.045147>. DOI: 10.1103/PhysRevB.109.045147.
- [37] JIA Y, YU J, LIU J, et al. Moiré fractional Chern insulators. I. First-principles calculations and continuum models of twisted bilayer MoTe<sub>2</sub>[J/OL]. Phys. Rev. B, 2024, 109: 205121. <https://link.aps.org/doi/10.1103/PhysRevB.109.205121>. DOI: 10.1103/PhysRevB.109.205121.
- [38] DEVAKUL T, CRÉPEL V, ZHANG Y, et al. Magic in twisted transition metal dichalcogenide bilayers[J/OL]. Nature Communications, 2021, 12(1). <http://dx.doi.org/10.1038/s41467-021-27042-9>. DOI: 10.1038/s41467-021-27042-9.
- [39] XIAO D, LIU G B, FENG W, et al. Coupled Spin and Valley Physics in Monolayers of MoS<sub>2</sub> and Other Group-VI Dichalcogenides[J/OL]. Phys. Rev. Lett., 2012, 108: 196802. <https://link.aps.org/doi/10.1103/PhysRevLett.108.196802>. DOI: 10.1103/PhysRevLett.108.196802.

- [40] GUO Y, PACK J, SWANN J, et al. Superconductivity in 5.0° twisted bilayer WSe<sub>2</sub>[J/OL]. *Nature*, 2025, 637(8047): 839-845. <http://dx.doi.org/10.1038/s41586-024-08381-1>. DOI: 10.1038/s41586-024-08381-1.
- [41] TUO C, LI M R, WU Z, et al. Theory of Topological Superconductivity and Antiferromagnetic Correlated Insulators in Twisted Bilayer WSe<sub>2</sub>[EB/OL]. 2024. <https://arxiv.org/abs/2409.06779>. arXiv: 2409.06779 [cond-mat.str-el].
- [42] GUERCI D, KAPLAN D, INGHAM J, et al. Topological superconductivity from repulsive interactions in twisted WSe<sub>2</sub>[EB/OL]. 2024. <https://arxiv.org/abs/2408.16075>. arXiv: 2408.16075 [cond-mat.supr-con].
- [43] XIE F, REGNAULT N, CĂLUGĂRU D, et al. Twisted symmetric trilayer graphene. II. Projected Hartree-Fock study[J/OL]. *Phys. Rev. B*, 2021, 104: 115167. <https://link.aps.org/doi/10.1103/PhysRevB.104.115167>. DOI: 10.1103/PhysRevB.104.115167.
- [44] XIE F, KANG J, BERNEVIG B A, et al. Phase diagram of twisted bilayer graphene at filling factor  $\nu = \pm 3$ [J/OL]. *Phys. Rev. B*, 2023, 107: 075156. <https://link.aps.org/doi/10.1103/PhysRevB.107.075156>. DOI: 10.1103/PhysRevB.107.075156.
- [45] BERNEVIG B A, SONG Z D, REGNAULT N, et al. Twisted bilayer graphene. III. Interacting Hamiltonian and exact symmetries[J/OL]. *Phys. Rev. B*, 2021, 103: 205413. <https://link.aps.org/doi/10.1103/PhysRevB.103.205413>. DOI: 10.1103/PhysRevB.103.205413.
- [46] YAMAMOTO J I, MOCHIZUKI Y. Optimal damping algorithm for unrestricted Hartree-Fock calculations[J/OL]. *Chem-Bio Informatics Journal*, 2014, 14(0): 14-33. <http://dx.doi.org/10.1273/cbij.14.14>. DOI: 10.1273/cbij.14.14.
- [47] ROOTHAAN C C J. New Developments in Molecular Orbital Theory[J/OL]. *Rev. Mod. Phys.*, 1951, 23: 69-89. <https://link.aps.org/doi/10.1103/RevModPhys.23.69>. DOI: 10.1103/RevModPhys.23.69.
- [48] SAUNDERS V R, HILLIER I H. A “Level-Shifting” method for converging closed shell Hartree-Fock wave functions[J/OL]. *International Journal of Quantum Chemistry*, 1973, 7: 699-705. <https://api.semanticscholar.org/CorpusID:97126829>.
- [49] ZANG J, WANG J, CANO J, et al. Hartree-Fock study of the moiré Hubbard model for twisted bilayer transition metal dichalcogenides[J/OL]. *Phys. Rev. B*, 2021, 104: 075150. <https://link.aps.org/doi/10.1103/PhysRevB.104.075150>. DOI: 10.1103/PhysRevB.104.075150.
- [50] WANG Z, KWAN Y H, WAGNER G, et al. Kekulé spirals and charge transfer cascades in twisted symmetric trilayer graphene[J/OL]. *Phys. Rev. B*, 2024, 109: L201119. <https://link.aps.org/doi/10.1103/PhysRevB.109.L201119>. DOI: 10.1103/PhysRevB.109.L201119.
- [51] KWAN Y H, WAGNER G, BULTINCK N, et al. Electron-phonon coupling and competing Kekulé orders in twisted bilayer graphene[J/OL]. *Phys. Rev. B*, 2024, 110: 085160. <https://link.aps.org/doi/10.1103/PhysRevB.110.085160>. DOI: 10.1103/PhysRevB.110.085160.
- [52] SCHEER M G, LIAN B. Twistrionics of Kekulé Graphene: Honeycomb and Kagome Flat Bands [J/OL]. *Phys. Rev. Lett.*, 2023, 131: 266501. <https://link.aps.org/doi/10.1103/PhysRevLett.131.266501>. DOI: 10.1103/PhysRevLett.131.266501.

## 致谢

本篇论文基于去年七月份开始对转角二硒化钨的数值研究，主要合作者为于家斌、胡昊昱、Dumitru Calugaru，分别从连续模型和紧束缚模型出发，互相印证。过去的讨论让我学到了很多，感谢我的合作者们。

特别感谢于家斌-也许现在可以叫师兄了。感谢你对我的毫无保留，无论是科研还是处事，都让我受益匪浅。今日得以忝列刘朝星老师门墙之下，实觉万幸。想来有些惭愧，最近这半年多，惶惶不可终日，心神难定，学术上的长进实在有限，对不住师兄的指导。希望博士期间，仍能多多讨论。

感谢我的本研指导老师宋志达，你让我知道了何谓“为人师表”，是我学习的榜样。感谢同在宋志达老师课题组的学长学姐们，能够与你们在同一个办公室学习工作，是我的幸运。从去年开始的昼夜颠倒的生活里，物院西 510 就是我的避风港。

感谢 304 宿舍的室友们，大伙儿既可以一块插科打诨，也可以一起讨论问题，让我的大学生活充实而又欢乐。还有我雅礼的同窗们，大家的情谊丝毫未减，感谢你们的倾听与陪伴。同样的感激，致以我常德的发小们，十多年的时光，我们一起走过。

感谢我的亲人们，这段时日实在太过艰难，你们春风化雨的关怀，让我铭记在心。在巨大的困难面前，我方才知道自己的不成熟与弱小。

将这篇拙作，献给我的父母。于我而言，你们是这个世界上最好的父亲与母亲。接下来赴美的留学生涯里，我会努力变成一个真正可以独当一面的人。一直以来都是我自顾自地谈论着自己的痛苦与愤懑，也许这只是一些青年人的无病呻吟罢了。我希望，你们也把自己的烦恼，和我一起分担。

有太多太多我想感谢的人；也有一些无法释怀、难以原谅的事情。但是，世间恩怨之事，原本难明，又何必喋喋不休？我本楚狂人，凤歌笑孔丘，学海无涯，那便纵一苇之所如，凌万顷之茫然。



# 北京大学学位论文原创性声明和使用授权说明

## 原创性声明

本人郑重声明：所呈交的学位论文，是本人在导师的指导下，独立进行研究工作所取得的成果。除文中已经注明引用的内容外，本论文不含任何其他个人或集体已经发表或撰写过的作品或成果。对本文的研究做出重要贡献的个人和集体，均已在文中以明确方式标明。本声明的法律结果由本人承担。

论文作者签名： 日期： 年 月 日

## 学位论文使用授权说明

(必须装订在提交学校图书馆的印刷本)

本人完全了解北京大学关于收集、保存、使用学位论文的规定，即：

- 按照学校要求提交学位论文的印刷本和电子版本；
- 学校有权保存学位论文的印刷本和电子版，并提供目录检索与阅览服务，在校园网上提供服务；
- 学校可以采用影印、缩印、数字化或其它复制手段保存论文；
- 因某种特殊原因须要延迟发布学位论文电子版，授权学校在  一年 /  两年 /  三年以后在校园网上全文发布。

(保密论文在解密后遵守此规定)

论文作者签名： 导师签名： 日期： 年 月 日